Experimental Observations of Tsunami Induced Scour at Onshore Structures

D. J. McGovern[a,*], D. Todd[b], T. Rossetto[d], R. J. S. Whitehouse[b], J. Monaghan[a], E. Gomes[c]

[a]*School of the Built Environment and Architecture, London South Bank University, 103 Borough Road, London, SE1 0AA, UK*
[b]*HR Wallingford, Howbery Park, OX10 8BA, UK*
[c]*CBCL Limited, 1489 Hollis Street, PO Box 606, Halifax, NS B3J 2R7, CANADA*
[d]*Department of Civil, Environmental and Geomatic Engineering, University College London, London, WC1E 6BT, UK*

Abstract

Tsunami inundation of the coastal environment can induce scour at structure foundations leading to failure. A series of experiments are made using a unique Pneumatic Long Wave Generator to generate tsunami wave periods of 25 - 147 s equating to 3 - 17.3 mins at 1:50 Froude scale. The waves propagate over a sloping bathymetry and impinge upon a square structure founded onshore in a flat sediment bed. Flow velocity, height and scour are recorded as a function of time during tsunami inundation. The rate of scour is observed to be time dependent. Equilibrium, which is not attained, is argued to be an inappropriate measure for time-dependent transient flows such as tsunami in which the flow velocity, depth and direction are variable. The maximum scour depth is recorded and critically is observed not to be equal to the final depth due to significant sediment slumping when flow velocities reduce in the latter stages of inundation. Current and wave scour predictor equations over predict the scour, while the ASCE 7-16 method under predicts. Comparisons with available data in the literature show longer inundation durations increase the amount of scour.

1. Introduction

Tsunami are commonly generated by under-sea mega-thrust fault motion or landslides, and contain sufficient potential energy to present a hazard to coastal life and the built environment. The 2004 Indian Ocean tsunami (IOT) resulted in over two hundred and fifty

---

[*]Corresponding author
Email address: `david.j.mcgovern1@gmail.com` (D. J. McGovern)

5 thousand casualties, $9.9 billion in material damage losses and 1.7 million displaced persons

6 (Telford et al., 2006). The 2011 Great Eastern Japan Earthquake and Tsunami (TET)

7 resulted in over fifteen thousand casualties and an economic impact of over of $211 billion in

8 direct damage (Kajitani et al., 2013). Scour is widely observed at, and often inferred as the

9 cause of failed coastal structures from post event field surveys (Chock et al., 2013; EEFIT,

10 2004, 2011; Mori and Takahashi, 2012; Yeh et al., 2007). In order to improve mitigation

11 against tsunami scour there is a need to understand its mechanism. This work presents

12 the first experimental study of onshore tsunami scour that considers tsunami inundation

13 time-scales appropriate to prototype. The results will pave the way to the development of

14 empirical models and to the validation of numerical models for predicting tsunami boundary

15 layers and scour at onshore structures.

16   When a structure is placed in a flow, scour may occur as a consequence of the boundary

17 layer interaction with the sediment and structure. This causes flow separations, vortex

18 formation and increased bed shear, all of which act to remove sediment until an equilibrium

19 between the turbulent flow field and the bed level is attained. Figure 1 shows a schematic

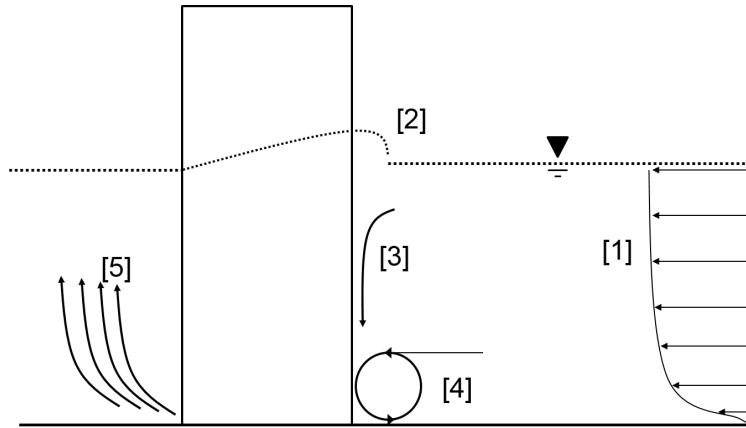20 diagram of the main scouring phenomena in waves and currents.

Figure 1: A schematic diagram of the flow field around a cylinder in a current or waves where [1] is the incoming flow velocity profile, [2] is the surface roller [3], is the downflow, [4] is the horse-shoe vortex, and [5] are the wake vortices (see for example Melville and Coleman 2000).

21   Finding the equilibrium scour depth for a given structure under a given flow condition

22 is of primary interest to the engineer because it informs design and mitigation. The scour

23 depth d_{sc} is often given as a non-dimensional scour depth d_{sc}/D (where D is the structure

24 diameter). In live-bed conditions (where flow velocity U exceeds the critical flow velocity

2

for sediment motion U_c), d_{sc}/D is shown to be a function of Keulegan-Carpenter number ($KC = \frac{UT}{D}$) by Sumer et al. (1992) (where U is the maximum induced bottom orbital velocity and T is the period of oscillation). At low KC numbers, the scouring flow field may not exist for long enough in time and space to significantly contribute to the scour process (Sumer et al. 2001a), and equilibrium may take longer to attain. At high KC numbers, where the flow is quasi-steady or steady, the scouring flow field is able to fully establish and equilibrium may be attained more quickly.

A vast quantity of literature and research exists on scour depth in waves, currents and combinations of waves and currents interacting with *offshore* and *wetted* (where the structure is sited permanently in a flow) structures. This research pertains to engineering applications in bridge pier design, and offshore structures. Reviews are given by Sheppard et al. (2014) for bridge pier scour and Sumer et al. (2001b) for offshore scour.

In the case of tsunami induced scour, the literature is more limited and field investigations of tsunami-induced scour are the primary source of scour data. Post-tsunami investigations of scour include Wilson et al. (2012) in harbours, Tonkin et al. (2013) at roads and structures, and Bricker et al. (2012) at coastal defences. Such retrospective investigations are few in number, geographically localised and infer only post-tsunami scour depths, extents and volumes; they are unable to provide systematic elucidation of the processes and mechanisms of scour evolution. As will be shown, the observed post-tsunami scour depth may not be equivalent to the maximum scour depth, and hence the use of such data may lead to non-conservative underestimations of the scour depth.

Experimentally, Yoshii et al. (2017) and Yoshii et al. (2018) investigated tsunami inundation and sediment transport and deposition in the coastal hinterland using two large wave flume studies. However, laboratory investigations of onshore tsunami scour at structures are very limited. Tonkin et al. (2003) uses solitary waves to represent tsunami at a circular cylinder. Nakamura et al. (2008) uses a combination of solitary and 'long waves' (with a maximum $T = 14$ s) for tsunami scour at a square cylinder. The solitary wave assumption does not allow for the period and length of the wave to be set independently, leading to unrealistic waveforms when scaled up to prototype (Madsen et al., 2008). Therefore, the appropriateness of the wave periods adopted in these investigations is limited, and may not be representative of prototype tsunami inundation. Nevertheless, Tonkin et al. (2003)'s experiments have been numerically simulated and applied to scour at bridge piers by Pan and Huang (2012) and this methodology is cited in the ASCE (2016) Chapter 6: 'Tsunami

Loads and Effects' design standards. Lavictoire (2014), Shafiei et al. (2015), Mehrzad et al. (2016) and Jayaratne et al. (2016), use a dam break method to generate tsunami-like bores. However, while bores may form on the surface of a tsunami wave as a consequence of soliton fission, for example, they represent only a small fraction of the tsunami period. As observed in experiments by Foster et al. (2017) and McGovern et al. (2018), when realistic tsunami periods are generated offshore, bore formation is rare, being tied to wave steepness λ/a, where a is the wave amplitude and λ is the wavelength. As described in McGovern et al. (2018) in an experimental study of tsunami runup, λ/a is extremely large for tsunami as compared to bores and shorter waves. They define a 'Relative Slope Length' parameter $\lambda \sin(\beta)/d$ (where β is the angle of the slope and d is the water depth at the point of wave definition) which describes the ratio of the length of the wave to the length of the slope over which it travels. For long waves such as tsunami, the parameter describes a situation where the wave is much longer than the slope and, therefore, shoaling is limited.

The scour research listed above, although addressing a multitude of different scenarios, can be grouped together by KC. As $KC \to \infty$ the oscillation is negligible and the flow is a steady current where $\frac{du}{dh}(t) = 0$ (where u and h are the instantaneous flow velocity and water height at the structures' location respectively and t is time). At low KC, $\frac{du}{dh}(t)$ is cyclic around 0 over a period defined by T.

Tsunami are characterised by periods of $\approx$ 90 s - 2 hrs (Brown, 2013) and their long periods translate into very long inundation events over land. Over shorter time scales, they can be assumed to exhibit quasi-steady currents (Foster et al., 2017). They are, however, cyclic over their defined period T, exhibiting variable flow velocities and inundation heights on land. The influence of a cyclic flow such as a tsunami on the boundary layer will be a combination of that of steady flows and waves. This is corroborated numerically by Larsen et al. (2017) and experimentally by Larsen et al. (2018) for tsunami induced scour at scaled offshore wind turbine monopiles. Therefore, it may be useful to describe tsunami by KC number when investigating its effect on scour.

Figure 2a shows a diagram of the model scale KC numbers investigated in the literature together with those for the experiments presented in this paper. KC number values between 50 and 1500 are expected for tsunami inundation flows, based on observations of the IOT and TET (flow velocity of $\approx$ 5 m/s full scale, Fritz et al. 2006, $D = 10$ m and a maximum period based on the TET of $T = 1260$ s, Kawai et al. 2013). On Figure 2a, it is observed that only the current experiments and Larsen et al. (2018) present tsunami specific studies

with KC numbers in this range.

Figure 2b shows the range of offshore wave period to amplitude ratios of the reviewed studies. The data of Chen and Li (2018), Sumer et al. (1992), Sumer et al. (2001a) are relevant to wind waves ($T \leq \approx 300$ s at full scale, Brown 2013). McGovern et al. (2014) and some of Sumer et al. (1992) are relevant to tides ($T \approx$ 12-24 hrs, at full scale). The tsunami-specific studies of Tonkin et al. (2003), Nakamura et al. (2008) and the shortest period used in the current study lie in the period range of 'short tsunami' ($T \leq \approx 180$ s). Few data exist in the 'long tsunami' region ($T \geq \approx 180$ s). The subdivision of 'short' and 'long' tsunami is proposed on analysis of Figure 10 in McGovern et al. (2018), in which the runup of long waves normalised by amplitude is plotted as a function of T. A distinct change in the shoaling behaviour of the waves is observed at $T \approx 100$ s, in which waves longer than this value do not appear to shoal significantly. That is, the 'Relative Slope Length' is so large that the incoming wave effectively sees the slope as vertical. The recorded period of the IOT ($T \approx 840$ s, the 'Mercator' profile, Rabinovich and Thomson 2007) and TET ($T \approx$ 1260 s), are both within the 'long' tsunami range and would have caused inundation periods that far exceed those generated at model scale by Tonkin et al. (2003) and Nakamura et al. (2008).
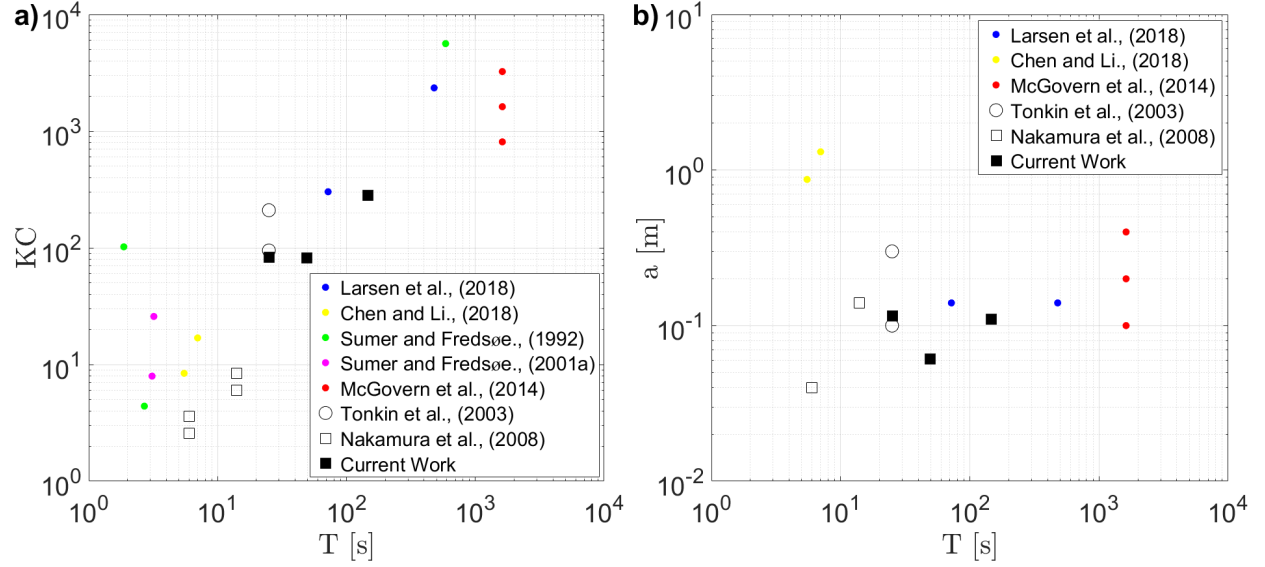
Figure 2: a) *KC* number regimes and b) the range of a as a function of T tested in the scour literature. Respectively, circular and square points depict circular and square shaped structures, filled and hollow points depict wet and dry sand at the structure and, large and small points depict onshore and offshore scour scenarios.

As scour is driven by the flow and turbulence field around a structure, it is important to assess its development due to an inundation flow with appropriately modelled $\frac{du}{dh}(t)$ that are specific to tsunami time-scales. To bridge the gap identified in the literature, these experiments investigate the scour development at an onshore square structure subject to cyclic inundation from transient flows of lengths and heights, which when scaled up are comparable to tsunami length inundation periods and amplitudes. First the experimental setup is presented. Next, the offshore and onshore hydrodynamics are described. Following this the scour development is described and compared to available scour prediction equations in existing tsunami codes and in the literature for steady currents and waves. A comparison of the scour data is then made with available data in the literature. Finally, a discussion of the limitations of the data is presented together with overall conclusions and recommendations for further work.

2. Experimental Setup

Cyclic inundation around model onshore buildings is produced using 1:50 Froude scaled crest and trough-led offshore waveforms generated by a Pneumatic Long Wave Generator

123 (PLWG), as described in Rossetto et al. (2011) and McGovern et al. (2018). Such waveforms
124 are analogous to full-scale tsunami in length and time scales. The PLWG, which in the
125 current set-up is a 4 m high, 3 m wide and 4 m long machined steel box, is placed at the far
126 end of the 75 m long, 4 m wide and 2.5 m deep 'Fast Flow Facility' flume at HR Wallingford,
127 U.K. Generated waves propagate along 23.9 m of constant depth followed by 20 m of 1:20
128 sloping bathymetry, before impinging and inundating on a 3 m long horizontal sediment
129 pit. This sediment pit is divided into three parallel bays by wooden bay splitters (Figure
130 3a-b). Interference from these bay splitters is minimised by using streamline tapers on the
131 leading edge. In the outer bays, a 0.2 m wide square perspex cylinder is placed normal to the
132 incident flow with the leading face 1 m downstream from the leading edge of the sediment
133 pit. These are termed 'Structure 1' (bay 1) and 'Structure 2' (bay 3) within this paper.
134 These represent 10 m x 10 m buildings at prototype scale, located 50 m from the shoreline.
135 Bay 2 contains a 0.4 m wide by 0.2 m long structure, the data of which is not reported here.
136 Due to the relatively low flow velocity in the reported tests, no interference in the overall
137 wave propagation over the test bed is observed due to the presence of the wider structure in
138 Bay 2. A fine, narrow graded sand ($d_{50} = 1.6 \ X 10^{-4}$ m, where d_{50} is the particle diameter
139 representing the 50% cumulative percentile within a sample of sand) of depth 0.8 m is used
140 in the pit and levelled flat before each test. Due to the low inundation depths associated
141 with the tsunami wave, the tests are relatively less sensitive to variations in particle size
142 than tests undertaken in deeper water as the critical threshold of motion varies slowly in
143 shallow water (e.g. at 0.1 m depth the variation in threshold between 0.1 - 0.7 mm sand
144 is $< 20\%$, see Soulsby and Whitehouse 1997). Therefore, this sediment can be considered
145 representative of a fine-to-medium sand. A rectilinear coordinate system is used with $X =$
146 0 m being the centre of the structure (1.1 m from the sea-ward edge of the sediment pit)
147 and negative towards the PLWG, Z being the vertical coordinate (0 m at the sand surface,
148 negative downwards) and Y being the lateral coordinate (set to 0 m at the centreline of each
149 structure in each bay, and negative towards the right from the perspective of the incoming
150 wave and towards the windows, Figure 3b-c).

151 Scour depth is measured using front-facing GoPro cameras inside each structure. GoPro
152 video is collected at 25 frames-per-second and analysed frame-by-frame to extract sand
153 elevations during tsunami inundation. This is used to determine the rate and depth of scour.
154 The scour depth around the edge of the structure, d_{sc}(X, Y, Z, t), is defined as the location
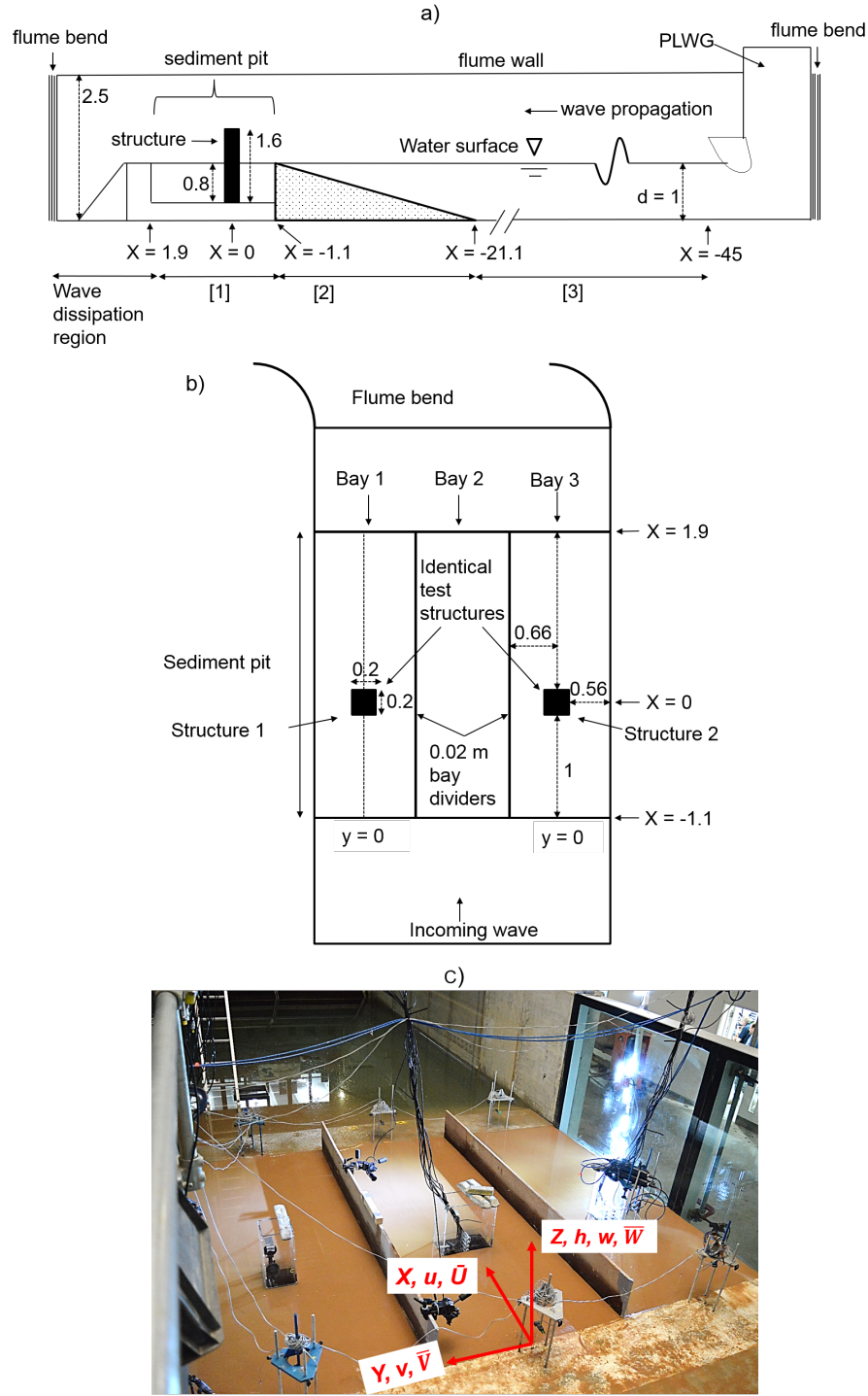155 of the sediment-fluid interface. The sediment-fluid interface is distinguished by eye from a

Figure 3: a) cross-sectional schematic of the flume with the onshore [1], near-shore [2] and offshore (constant-depth) [3] regions shown, b) top view of sediment pit region, c) the coordinate system used annotated on a digital picture of the flume test section. All dimensions are in metres (not to scale).

visible change in colour, on individual still frames of the GoPro video (for example, Figure
4). These data points are defined in the X and Y planes against a 0.01 m scale grid drawn
onto the front and side faces of each structure. This allows d_{sc} to be recorded at 0.01 m
intervals along the Y and X planes for the front and side of the structure respectively. The
Z grid is scaled to 0.005 m in the X, Y and Z planes. During analysis on a computer, an
additional grid is added to the screen to refine the scale to 1 mm, thereby giving an accuracy
of ± 0.0005 m in the X, Y and Z directions. Normalising the coordinates by D, $d_{sc}(t)$ is
measured on the front faces of the structures (positioned at X = -0.1 m) from Y/D = -0.45
to Y/D = 0.4 every $0.05D$, giving 18 data points. On the right side faces of the structures,
(as viewed on Figure 3b, corresponding to Y = -0.1), $d_{sc}(t)$ is recorded every $0.05D$ from
X/D = -0.45 to X/D = 0.45, giving 19 data points. d_{sc} is recorded at a frequency of $T/20$
for each wave type (accuracy $\pm$ 0.04 s), starting when the wave front first reaches X = -0.1
m, and continuing for up to $1.5T$. Visual analysis is straight-forward when the suspended
sediment concentration near the interface is low to medium. However, in periods of vigorous
scour, the fluid-sediment interface becomes blurred, leading to an increased uncertainty in
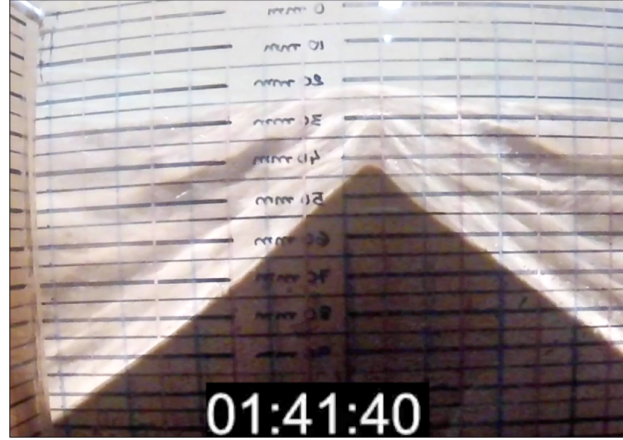the measurement. This will be discussed further in Section 3.2.

Figure 4: Example of a raw GoPro video frame on the leading face of the structure with the 0.01 m X
grid and 0.005 m Y grid. An additional 0.001 m grid is individually added to the screen during manual
processing.

Time-dependent free-surface elevation along the flume $\eta(X, t)$ is recorded using resistance-
type wave gauges (accuracy $\pm$ 0.0005 m, manufactured by HR Wallingford). These are placed
at 5 m intervals from X = -38.64 m to -13.64 m and then at -2.54 m. Eight wave gauges
are placed at various locations in the sediment pit, dependent on the individual test. Flow

velocities are measured at X = -21.1 m using a Nortek HR Aquadopp and over the sediment pit using two Nortek Vectrino II profilers. The Aquadopp face is 0.06 m from the fixed concrete bed and faces upwards. Velocity profiles are recorded at 1 Hz and are extended to the surface and bed using an exponential fit. Velocities are depth-averaged to produce a time series. The Nortek Vectrino II profilers record velocities at 25 Hz in the X, Y, and Z directions. A Reynolds decomposition gives the mean velocity components.

The sediment pit walls are porous meaning these tests are in the wet regime. The water level is constantly set to the lip of the pit throughout the test campaign preventing any desaturation. It is noted that the wet regime may not always occur in the prototype during the first inundation of a tsunami, but may be applicable to subsequent waves. The potentially increased relative scour of a wet model due to the higher pore-water pressure in comparison to a dry prototype will lead to conservative results. Before each test run, the saturated sand is flattened and the GoPro cameras inserted with WiFi control enabled, allowing single synchronous remote control. The PLWG is switched on and after a short period of settling time, the test is conducted and the scour, velocity and η are recorded.

The test conditions as recorded at X = -1.1 m (X/D = -5.5) are given in Table 1. This position corresponds to the upstream lip of the sediment pit. The origin of the parameter values are described in Section 2.2. Before this in Section 2.1, the characteristics of the offshore waveforms that propagate over the sloping bathymetry before inundating over the sediment pit are described.

2.1. The offshore waveform

The offshore waveforms generated include crest-led waves of T = 25 s (CL25) and 147 s (CL147) and a trough-led wave of T = 49 s (TL49). Tsunami have been observed to exhibit both crest-led and trough-led shapes, for example see Tadepalli and Synolakis (1994) and Madsen et al. (2008). Figure 5a-c shows free surface elevation η at X/D = -23.64 m as a function of t (where, $t = 0$ is the start of the PLWG wave generation cycle, which includes 60 s of still water before the wave begins) for the CL147a, TL49a and CL20a tests. Each are typical of the relevant wave periods. From Figure 5a-c, the periods of each wave are defined as $T = t_{end} - t_{start}$ where t_{start} and t_{end} are defined as the times at which $\eta(X,t)$ first up-cross and down-cross the value corresponding to 1% of a respectively (see also McGovern et al. 2018). X = -23.64 m is the wave gauge in the offshore region nearest to the bathymetry toe, and represents the position at which the waveforms are calibrated. This position is chosen as

it represents a location where reflections from the slope are manifest almost instantaneously on the waveform, and it constitutes a definitive change in slope that is easier to define in a prototype. Due to the very long wavelengths of the waves being produced, their recording at any given point in the flume may be a composite of the incident and reflected components, the main source of the reflection being the sloping bathymetry. The definition point is discussed in detail in McGovern et al. (2018), who also show that the PLWG effectively absorbs reflections from the slope.

The crest-led waves produced by the PLWG are much longer than the theoretical solitary waveform given by Equation 1. Clearly, the short inundation time that occurs from a solitary wave will not result in the long period scour regime that would be expected for a tsunami-like inundation. The trough-led wave is plotted against the theoretical N-wave (Equation 2) and the sine function $\eta(t) = a^+ \sin(2\pi f t)$, where f is frequency. The measured wave is longer and shallower than the N-wave, and more closely matches the sine waveform.

$$\eta(X, 0) = \frac{H}{d} \operatorname{sech}^2(K_s(X - X_1)) \tag{1}$$

where $K_s = 1/d\sqrt{3H/4d}$, and H = wave height.

$$\eta(X, 0) = \alpha \frac{H}{d}(X - X_2) \operatorname{sech}^2(K_s(X - X_1)) \tag{2}$$

where α is a constant, X_1 is the position the crest and X_2 is the horizontal position of the zero-crossing point in the wave profile.
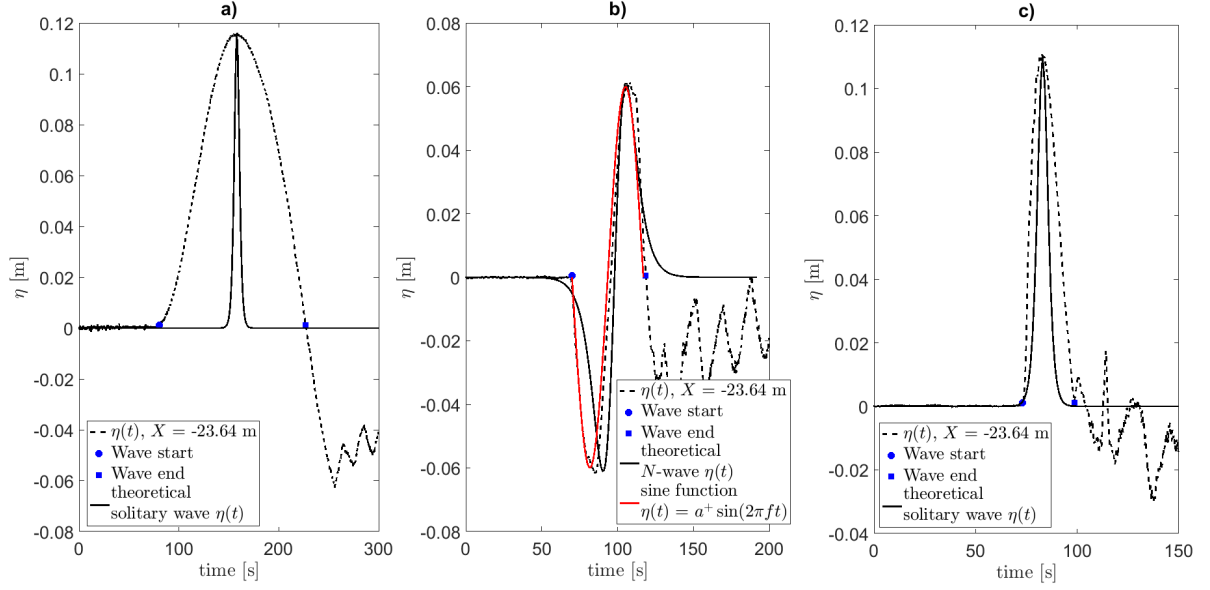
Figure 5: a-c measured $\eta(X)$ as a function of t for the CL147, TL49 and CL25 waves respectively. The CL waves are compared against the theoretical solitary waveform, while the TL49 wave is compared against the theoretical N-wave and sine function.

The Aquadopp velocity data recorded at $X = $ -21.1 m is presented in Figure 6a-f, with a), c) and e) showing the streamwise u velocity profile as a function of t/T and b), d) and t) the depth-averaged velocity $\bar{U}$ and free-surface η for the CL147a, TL49a and CL25a waves respectively. At $X = $ -21.1 m the velocity profiles are 2-dimensional, with minimal $\bar{V}$ component. The occurrence of maximum velocity, $\bar{U}_{max}$ and maximum free surface, η_{max}, are out of phase. $\bar{U}_{max}$ occurs at $\approx \frac{2}{3}$ of η_{max}, at which point $\frac{d(\eta)}{d(t)}$ is also approximately at its maximum. This corroborates the time at which inferred overland maximum velocities occur from video analysis of the TET as used in the ASCE (2016) design standard (Figure 6.8-1 therein) to calculate the onshore tsunami flow velocity at a given inundation height. The velocity-height data presented here provides experimental confirmation of this relationship. The phase difference between $\bar{U}$ and η means that towards the end of the wave, $\bar{U}$ becomes negative, representing a return flow.
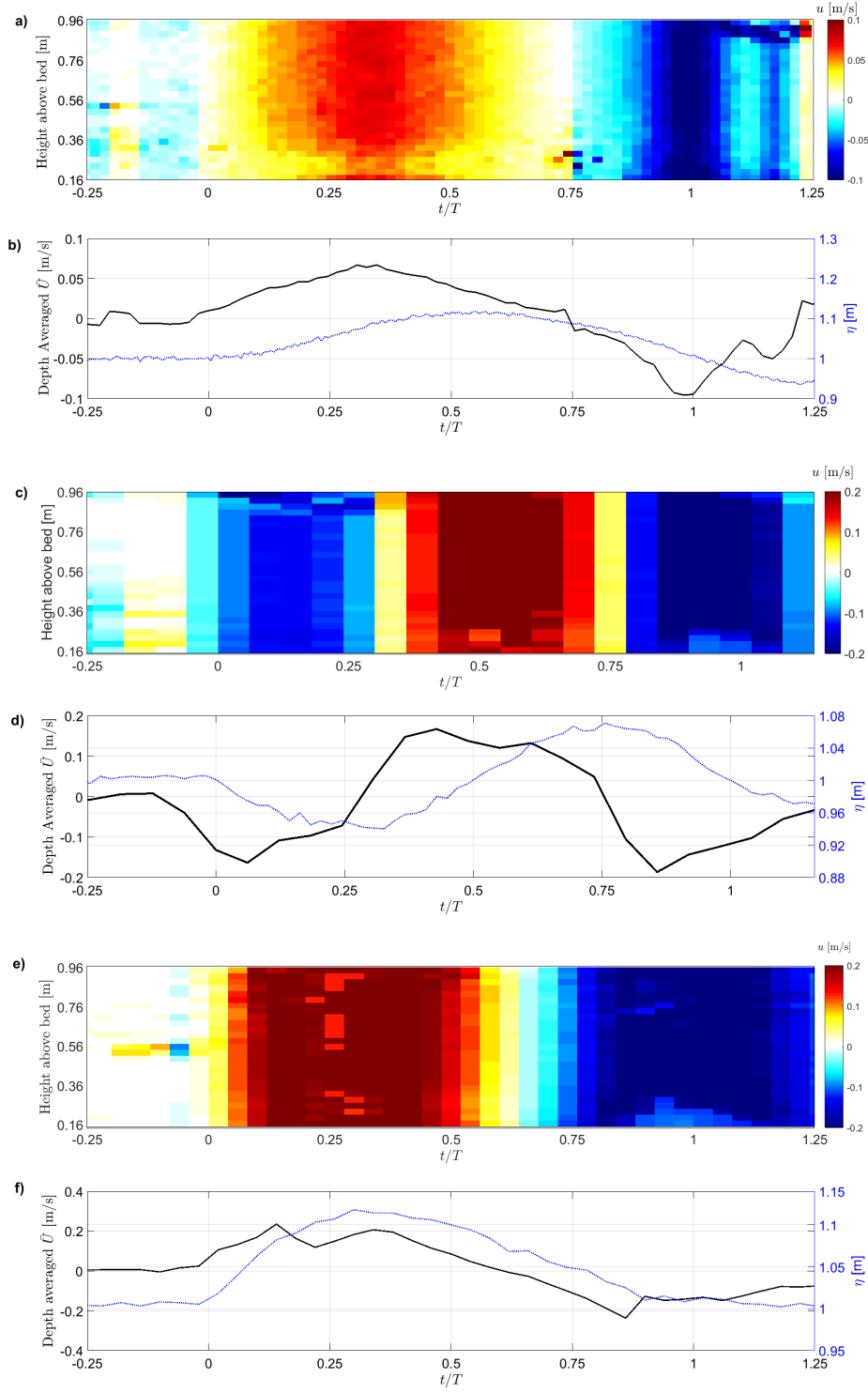
12

Figure 6: a-f. Aquadopp velocity data recorded at $X = $ -21.1 m where a), c), e) shows the u velocity profile as a function of t/T for the CL147a, TL49a and CL25a respectively and b), d), f), the depth-averaged velocity $\bar{U}$, and free surface height η [m] as a function of t/T, for the CL147a, TL49a and CL25a respectively. The noise at ≈ 0.9 m above the bed after $t/T \approx 1.25$ on a) is due to the water surface.

13

2.2. The onshore inundation characteristics

The offshore waveforms described above propagate over the sloping bathymetry before impinging on the test bed and structure. This inundating flow velocity and height are not equal to the offshore values. Table 1, therefore, gives the onshore values at the position $X = -1.1$ m as these values are more useful in relating to the onshore scour. The value of $\bar{U}_{max}$ in Table 1 is the maximum onshore value extracted from the Vectrino profilers. The Vectrino's record the bottom 0.035 m of the flow depth which means that the $\bar{U}_{max}$ given is likely to be lower than $\bar{U}_{max}$ averaged over the whole flow depth. This value is used in the KC calculation instead of the offshore value recorded by the Aquadopp as the flow velocity significantly increases onshore, and the appropriate KC number relating to the scour at the structure is that calculated from the parameters nearest the structure. For tests CL147b and CL147c the Vectrino is moved to a near-structure location, so there is no value for $\bar{U}_{max}$ at $X = -1.1$ m. However, it is assumed that as the offshore waveform is the same, the onshore flow is likely similar. Therefore, the values of Reynolds Number $R_h = \frac{\rho \bar{U}_{max} h_{max}}{\mu}$, (where h_{max} is the maximum onshore inundation height, ρ the density of water = 1000 kg m^3 and μ is the dynamic viscosity of water = 1.307 $\times 10^{-3}$), Froude Number $Fr = \frac{\bar{U}_{max}}{\sqrt{gh_{max}}}$, and KC from CL147a are assumed to represent CL147b-c as well. The Shields parameter is calculated using the expressions provided in Fuhrman et al. (2013), reproduced in Equation 3.

$$\theta = \frac{U_{fm}^2}{(s-1)gd_{50}} \tag{3}$$

where U_{fm} is given by

$$U_{fm} = \sqrt{\frac{f_w}{2}} U_{max} \tag{4}$$

where f_w is the friction factor. Hydraulically smooth conditions prevail in the CL147, TL49 and CL25 waves as $ks^+ = (ks\, U_{fm})/\nu$ does not exceed 10, where ks is the Nikuradse roughness equivalent for the sand used, and ν is the kinematic viscosity of water. Thus f_w is given by Fuhrman et al. (2013) as

$$f_w = 0.04Re^{-0.16} \tag{5}$$

and is shown to be a reasonable estimate for use with tsunami by Williams and Fuhrman (2016). Here, $Re = \frac{aU_{max}}{\nu}$, where $a = \frac{U_{max}T}{2\pi}$. For hydraulically rough conditions Williams

and Fuhrman (2016) suggest Equation 6.

$$f_w = exp\left(5.5\left(\frac{a}{ks}\right)^{-0.16} - 6.7\right) \tag{6}$$

This method is also employed by Larsen et al. (2018) for their offshore tsunami cases. Table 1 provides the Shields parameter $\theta_{onshore}$ as calculated at X = -1.1 m, i.e., the value in the vicinity of the structure. The critical Shields parameter for incipient sediment motion $\theta_{cr} = 0.055$ is given by the method outlined in Soulsby and Whitehouse (1997), Equation 7.

$$\theta_{cr} = \frac{0.3}{1 + 1.2d_*} + 0.055(1 - exp(-0.020d_*)) \tag{7}$$

where dimensionless grain size d_* is given by Equation 8.

$$d_* = \left[\frac{g(s-1)}{\nu^2}\right]^{\frac{1}{3}} d_{50} \tag{8}$$

Additionally on Table 1 the number of front (small 'f') and side (small 's') scour depth data sets recorded is given. In some tests, GoPro failures prevented the collection of usable scour data.

Table 1: Key wave parameters at X = -1.1 m and the number of scour data sets obtained

Run	T [s]	$\bar{U}$ [m s^{-1}]	maximum h [m]	R_h	Fr	KC	$\theta_{onshore}$	$\frac{\theta}{\theta_{cr}}$	scour data sets
CL25a	25	0.666	0.207	1.05×10^5	0.47	83	0.8	12.7	2f, 1s
CL25b	25	0.666	0.208	1.06×10^5	0.47	83	0.8	12.7	2f, 1s
TL49a	49	0.324	0.121	2.99×10^4	0.30	79	0.16	2.48	2f, 1s
TL49b	49	0.334	0.119	3.04×10^4	0.31	82	0.17	2.62	2f, 1s
CL147a	147	0.382	0.093	2.72×10^4	0.40	281	0.22	3.50	1f, 2s
CL147b	147	-	0.09	2.63×10^4	0.41	281	0.22	3.51	1f, 1s
CL147c	147	-	0.093	2.72×10^4	0.40	281	0.22	3.5	1f, 1s

From Table 1, the equivalent full-scale sediment grain size is 9.7 mm for the CL25 wave condition, when similitude in flow intensity U/U_c is attained between the model and prototype. For all waves, the prototype Reynolds numbers are 2 orders of magnitude larger leading to turbulent wake formation in both the model and prototype.

3. Results

3.1. Flow Characteristics around an Onshore Structure

277 Scour is caused by the change in the free-stream flow field by the presence of a structure.
278 In unidirectional currents and waves, this flow structure is relatively well defined. It is a
279 reasonable hypothesis to assume that the instantaneous flow field around a structure during
280 tsunami inundation is analogous to that of a steady current, and similar arguments are made
281 for tidal flows at offshore structures (e.g., Whitehouse 1998 and McGovern et al. 2014). The
282 caveat is that this would only apply to boundary layers that extend over the entirety of the
283 flow depth, as Williams and Fuhrman (2016) and Larsen et al. (2018) show the tsunami
284 boundary layer may also exhibit wave-like characteristics. This section discusses the onshore
285 flow characteristics in an attempt to verify this hypothesis. In this section all X, Y and Z
286 positions are normalised by D. Instantaneous time t is normalised by period T, where t/T
287 = 0 denotes the time at which the wave start is recorded at the respective position.

288 Figure 7a shows streamwise $\bar{U}$, lateral $\bar{V}$ and vertical $\bar{W}$ onshore velocities at onshore
289 locations in Bay 3 around Structure 2, where X/D = -5.5, taken by a single Vectrino II
290 profiler during test CL147a. Figure 7b shows the same onshore velocities at X/D = -1.1
291 and -1.175 taken simultaneously by a pair of Vectrino II profiles during test CL147b (see
292 legend for full coordinates). The onshore water depth $h(t)$ recorded at X/D = -5.5, Y/D
293 = 0 (the centreline) for the CL147a and CL147b wave runs is also given in Figure7a-b,
294 respectively. There is good agreement between experimental runs in $h(t)$. The delay in the
295 velocity record compared to $h(t)$ is due to the flow depth being below the Vectrino transducer
296 head. Vectrinos are advantageous for boundary layer measurements over counterparts that
297 may be deployed, due to their low profile and ability to provide non-invasive measurements
298 beyond the effects of the probe head (defined by the blanking distance). Additionally, they
299 are able to measure a flow profile from which the depth-averaged velocity may be derived.
300 It should be noted that the profiler transducer head begins each experiment exposed to air
301 before being submerged. Readings only occur for $h \geq$ transducer head height.

302 h at X/D = -5.5 is lower ($h_{max} \approx 0.093$ m) than at X/D = -118.2 (i.e., X = -23.64
303 m, where $h_{max} \approx 0.11$ m, see Figure 6b) due likely to the acceleration of the flow over the
304 onshore region indicating a transition from wave to current-like flow. $\bar{U}$ at X/D = -5.5
305 (Figure 7a) decreases with time from a peak of 0.38 m/s corresponding to $\approx \frac{2}{3}h_{max}$, again
306 in agreement with Figure 6b and ASCE (2016). This scales up to ≈ 2.7 m/s at 1:50. Field
307 measurements of tsunami overland velocities have been shown to be in the region of 2 - 5 m/s
308 (Fritz et al., 2006). On Figure 7b $\bar{U}_{max} \approx 0.4$ m/s is recorded at X/D = -1.1, Y/D = -0.5 (in

line with the corner of the structure), due to flow constriction along with significant negative $\bar{V}$ (describing flow to the right of the incident wave direction, towards the flume wall, Figure 3b), due to the deflection of incoming flow across the front face of the structure. It should be noted that unlike elsewhere in the monitored onshore and nearshore regions, $\bar{U}_{max} \approx 0.4$ m/s at the leading corner of the structure (X/D = -1.1, Y/D = -0.5) occurs in-phase with h_{max}. This observation appears to contradict the guidelines in ASCE (2016). At X/D = -1.175, $Y/D = 0$, $\bar{U}$ reaches a maximum at $\approx \frac{2}{3}h_{max}$ as seen in Figure 7a, but reduces in a more non-linear manner in the latter stages of the inundation. The variation indicates the relatively turbulent nature of the flow in this region which is due to the presence of a growing scour hole affecting the flow near and at the bed. $\bar{V}$ is zero as expected at the centreline, and $\bar{W}$ is slightly negative due to the presence of the downflow closer towards the structure.
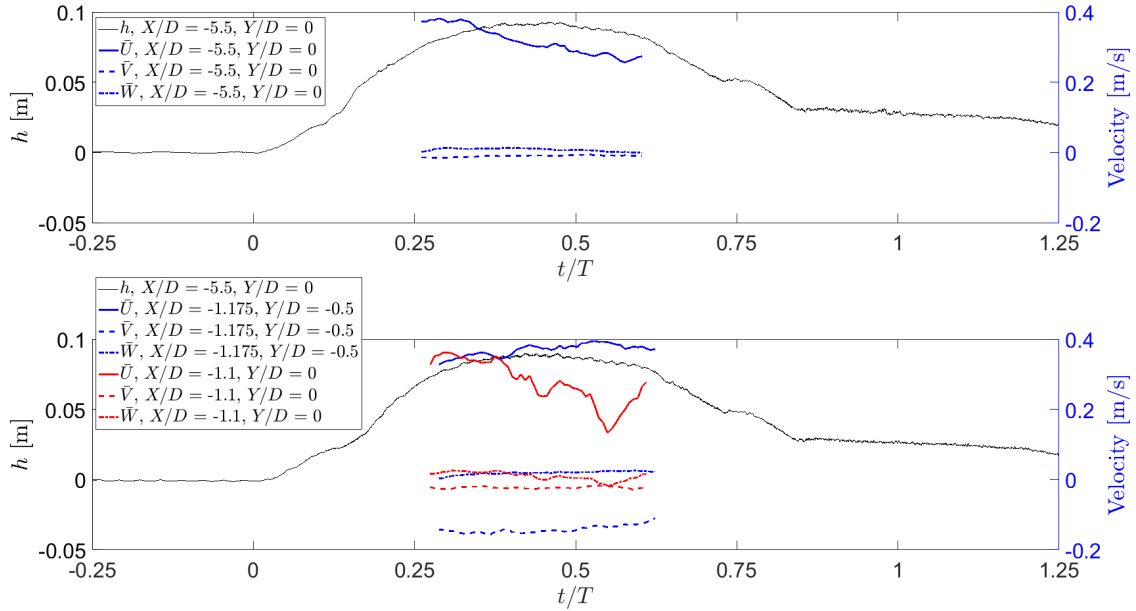

Figure 7: a) h (m, left y axis), $\bar{U}$, $\bar{V}$ and $\bar{W}$ (m/s, right y axis) as a function of t/T at X/D = -5.5, Y/D = 0 during CL147a, and b) during CL147b at X/D = -1.175, Y/D = -0.5, and X/D = -1.1, $Y/D = 0$.

The equivalent $\bar{U}$, $\bar{V}$ and $\bar{W}$ as a function of t/T for the TL49 and CL25 waves is not available due to a failure of the synchronisation signal between the wave gauge data acquisition and the Vectrinos. While time series velocity data exists it cannot be matched with the time series wave gauge data with certainty. However, the maximum values can be reported (Table 1).

3.2. Tsunami Induced Onshore Scour

17

The time development of scour is now discussed beginning with the CL147 wave which is repeated three times (CL147a, b and c, see Table 1). There is good agreement in the following discussion of the recorded scour process from the side and front views of the structures for all wave runs. Hence for brevity, the detailed process of scour is discussed only in relation to Structure 1 and CL147a.

Figure 8a-j shows video image stills of the scour development at the front and side of the structure at selected instances of the inundation. Here, $t/T = 0$ denotes the time at which the wave front first impinges on the structure. The estimated duration and delineation of flow direction in the inundation process is made from examining individual video frames. Flow direction is onshore between $t/T = 0$ - 0.845 after which flow reversal occurs.
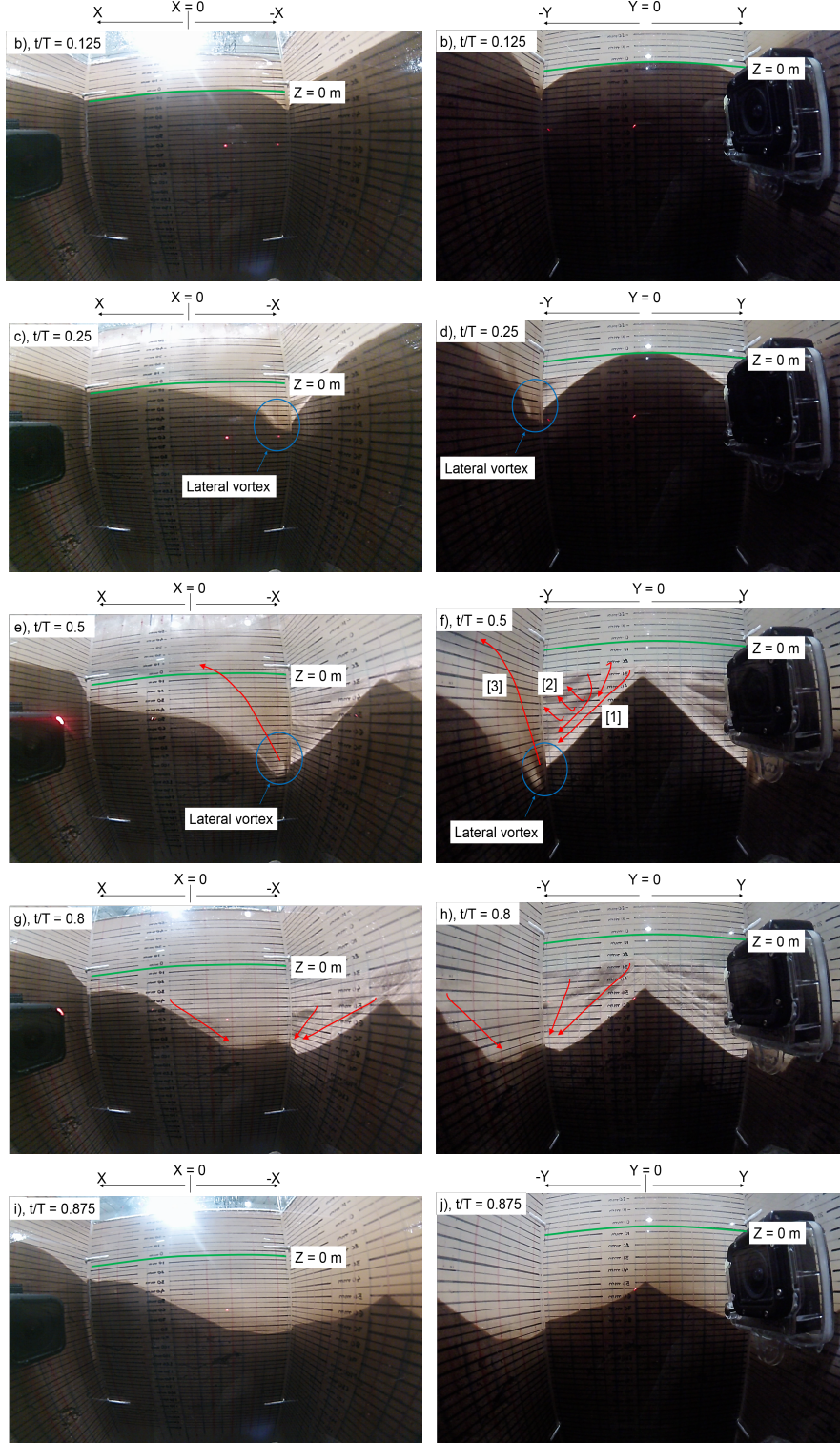
Figure 8: GoPro video stills from inside Structure 1 at variable intervals from the start of inundation during CL147a selected to highlight the scour process. The left and right columns show progressively $t/T \approx 0.125$, 0.25, 0.5, 0.8 and 0.875 for the side and front views respectively. Refer to the text for explanations of the annotations.

Figure 9a-b shows the time development of scour along the side face and front face respectively during the inundation process for Structure 1 during CL147a. The scour depth d_{sc} is plotted at 6 s intervals ($t/T = 0.043$) from $t/T = 0$ and as a function of X/D for the side face (Figure 9a) and Y/D for the front face (Figure 9b). The minor offset of the initial bed level from zero observed in Figure 9a-b at $t/T = 0$ is within experimental error and no obvious bias in the scour depth appears to be carried forward into the later stages of scour development. Bed levels can only be extracted at the sediment-water interface when there is a strong contrast in light and dark between the water and the sediment. During the experiment instantaneous changes in the lighting and reflection during the scour development lead to losses in data. The region between X/D -0.45 to -0.5 and 0.45 to 0.5 on Figure 9a and between $Y/D \approx$ -0.5 to -0.45 on Figure 9b contain no data as light refraction from the side panel of the perspex structure distorts the GoPro image preventing the distinct contrast between sand level and water column. There is no data between $Y/D \approx$ 0.4 to 0.5 for similar reasons. Additionally, as sharpness of the fluid-sediment interface varies depending on the instantaneous conditions of the flow and suspended sediment concentration, the error in d_{sc} recorded at any position varies through the inundation. This error increases from t/T $\approx$ 0.2 to t/T $\approx$ 0.5, when depth-averaged flow velocity $\bar{U}$ is relatively high (Figure 7), and the vigorousness of scour is greatest (for example, Figure 8e and f). The scour analysis in this paper focuses on the maximum scour depth, $d_{sc,max}$, which occurs in the region $0.55 < t/T$ <0.80; and the final scour depth, $d_{sc,end}$, that occurs at $t/T > 1$. $d_{sc,end}$ is the end scour depth recorded as the mean value after the change in d_{sc} becomes less than 1% of the current value. During these times $\bar{U}$ is reduced and suspended sediment load is decreased, meaning the sediment fluid boundary is distinct, giving an accuracy $d_{sc} \pm 0.001$ m, (less than <1% of the maximum d_{sc}).
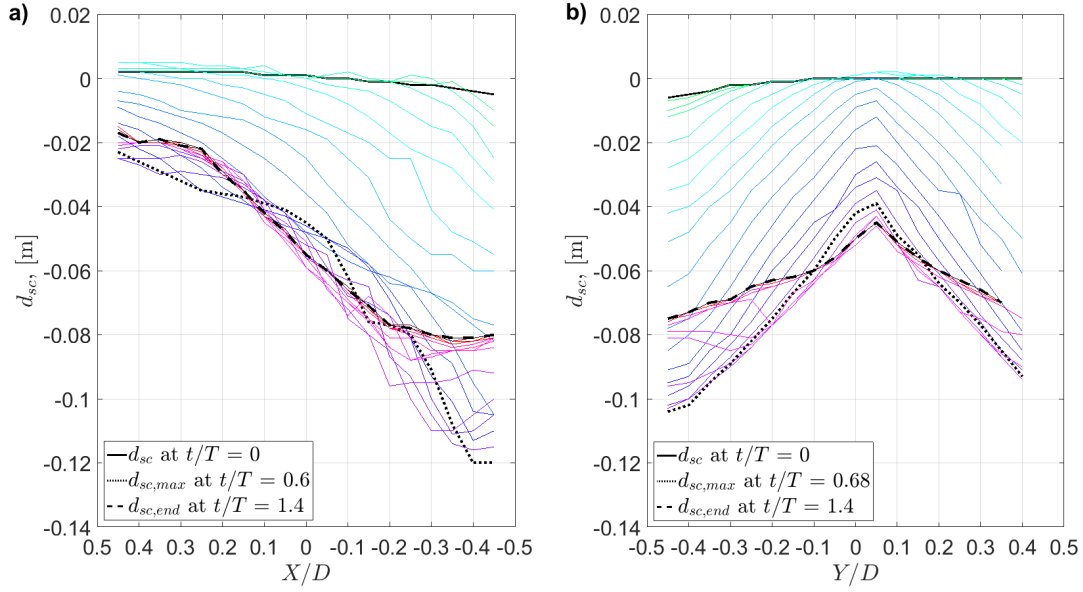
a)

d_{sc}, [m]

0.02
0
-0.02
-0.04
-0.06
-0.08
-0.1
-0.12
-0.14

— d_{sc} at $t/T = 0$
···· $d_{sc,max}$ at $t/T = 0.6$
-- $d_{sc,end}$ at $t/T = 1.4$

0.5 0.4 0.3 0.2 0.1 0 -0.1 -0.2 -0.3 -0.4 -0.5
X/D

b)

d_{sc}, [m]

0.02
0
-0.02
-0.04
-0.06
-0.08
-0.1
-0.12
-0.14

— d_{sc} at $t/T = 0$
···· $d_{sc,max}$ at $t/T = 0.68$
-- $d_{sc,end}$ at $t/T = 1.4$

-0.5 -0.4 -0.3 -0.2 -0.1 0 0.1 0.2 0.3 0.4 0.5
Y/D

Figure 9: a-b. The development of scour at the side a), and front faces b) of Structure 1 CL147a wave. Bed level readings are taken every 6 s ($t/T = 0.04$). The time at which $d_{sc,max}$ and $d_{sc,end}$ are achieved is highlighted. The small variation of the initial bed level around zero does not appear to have any significant impact on the scour development, which is qualitatively similar to the CL25 and TL49 tests (see Figures 11a-d) maxima and end depths.

The following discussion refers to both Figures 8a-j and 9a-b. The scour initiates at the corner of the structure, gradually moving towards the centreline where scour initiates $\approx$ 40 s later ($t/T = 0.27$). On the front face the scour hole forms, and retains until the end of the test, a triangular shape with the apex located on the centreline. This is indicative of the early stages of scour development at a square structure (for example, Sumer et al. 1993). Along the side face scour also begins at the corner moving gradually downstream along the structures edge (in agreement with Nakamura et al. 2008 and Shafiei et al. 2015). The largest scour depth is observed at the corner and is due to a strong vortex generated by lateral boundary layer separation from the structures edge. This vortex is observable in the videos and in Figure 8c-f in particular (see annotations). In studies of air-flow past a square cylinder, this type of vortex has been termed a base-vortex (for example Saha 2013). From the observation of the videos, impinging water on the front face is deflected down and away from the centreline following the triangular shape of the scour hole. The general behaviour of the scour process is most readily apparent in Figures 8e-f. The process appears

21

to be primarily dominated by the lateral vortex energetically removing sediment from the corner. The movement of sediment through the scouring region can be grouped into three observed behaviours. These are illustrated by three sets of red arrows in Figure 8e-f which indicate the observed movement of sediment. Additionally, these features are represented schematically on Figure 10a-b. Movement of sediment towards the corner of the structure is observed from upstream of the leading lip of the scour hole, the sides of the scour hole and from the centreline apex, which in three-dimensions is a ridge (Figure 8f arrows [1]). This sediment is then suspended by the lateral vortex and carried downstream by the prevailing flow past the structure [3]. [1] is bounded by a distinct region that is farther away from the centreline where sediment is suspended via a different process to the lateral vortex and carried laterally outwards and then downstream [2]. This may be elements of a horseshoe vortex forming from the separation of the upstream bed boundary layer at the lip of the upstream scour hole.
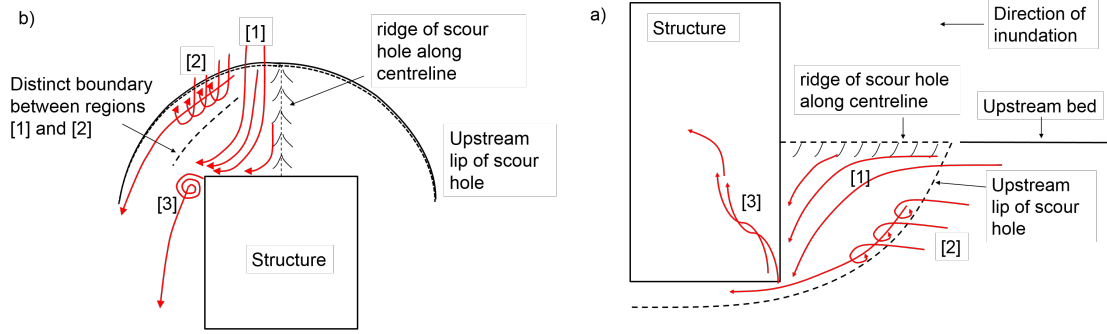

Figure 10: Schematic representations of the scour process as depicted in Figure 8e-f at $t/T = 0.5$ from the a), top down and b), side views respectively.

As shown by Hjorth (1975), the leading corner is the position of greatest bed shear stress amplification, while the centreline exhibits bed shear amplification ≈ 1. This would explain the delay in scour along the centreline. This delay indicates that the horseshoe vortex is not likely to be a strong influence on the early stages of the scour process, as if it were, the observed delay would be much less. At wetted circular structures, the scour process also begins laterally before quickly migrating towards the front as the downflow and horseshoe vortex establish themselves as the dominant mechanism (for example, Ettema 1980, Melville and Coleman 2000). The horseshoe vortex may participate more in the later stages of inundation, though the lack of suspended sediment observed in the front face

throughout Figure 8 suggests that it remains a secondary scouring phenomena, and forms further upstream of the structure from the separation over the scour hole upstream lip. For the duration of a single inundation as generated here, the scour mechanism appears to be dominated by the lateral vortex.

$d_{sc,max}$ = 0.12 and 0.104 m occurs at t/T = 0.6 and 0.68 on the side and front faces respectively. Once $d_{sc,max}$ is achieved, backfilling occurs at the corners due to sediment slumping. In Figure 9a the majority of the slumping occurs between X/D = -0.45 to -0.25 on the side face and Y/D =-0.45 to -0.1 on the front face. The maximum slope angles of the bed observed on the side and front faces when $d_{sc,max}$ occurs is 84.3° and 81.4°, respectively. The majority of the slumping along the side face occurs between t/T = 0.69 - 0.81 due presumably to the flow velocity dropping below the velocity threshold required to maintain a steeper slope. The natural angle of repose of the sediment is 31°. Beyond these regions $d_{sc,max} \approx d_{sc,end}$, suggesting that the slumping sediment originates from the sides of the scour hole collapsing in towards the structure. Along the front face a 0.031 m decrease in depth occurs between $\approx t/T$ = 0.68 - 0.82. The slight delay in slumping at the side wall may be due to the lateral vortex retaining its identity slightly longer than the scouring phenomena at the front face (horseshoe vortex and downflow), due to the sharp separation edge provided by the structures' corner. This can be observed in Figures 8g-h which shows some suspended sediment and a vortical structure at the side face at t/T = 0.8. While no onshore velocity record is available at this point due to the reduction of h below the Vectrino transducer heads, an inference can be made from the offshore velocity. Figure 6b shows that offshore velocities will approach zero and reverse after t/T = 0.75 ($\approx \frac{3}{4}T$), thus the period between t/T = 0.68 - 0.85 onshore can be assumed to coincide with the occurrence of velocities approaching zero. This is further corroborated by visual analysis of the GoPro videos, with Figure 8h displaying a major slumping event at the front face at t/T = 0.8 occurring with low suspended sediment indicating lower flow velocities (as also observed during playback). This image and playback shows that the slumping of sediment occurs from the sides of the scour hole slumping in towards the structure as well as along the structures' surface. The slumping is staggered in time with a second event backfilling the region between the corner and centreline at approximately t/T = 0.8 - 0.86, (Figures 8j and 9b).

Figure 8i-j, taken at t/T = 0.875 during the return flow shows significant suspended sediment in what is now the rear of the structure relative to the flow direction. This implies that the scour process is now reversed. Hence, the four distinct sediment transport phases

23

that appear to occur during the inundation process may be identified as: 1) initial local scour during inundation, 2) backfilling from maximum scour depths during inundation and flow reversal, 3) local scour due to the return flow and, 4) backfilling towards and beyond the end of the return flow.

Figure 11a-d shows the scour time development for the side (a and c) and front (b and d) of the structure during the TL49a and CL25a waves respectively. Similar to the CL147a wave, scour begins at the corners. At the front, the scour develops in much the same way with a triangular bed level with the apex at the centreline, and significant slumping occurs towards the end of the waves. The side views have a similar shape with the deepest scour depth occurring at X/D = -0.45. Slumping, however, is much smaller than observed for the CL147a wave. The scour process appears much the same as for the CL147a wave, however, the horseshoe vortex, which rotates clockwise, is more apparent particularly in the early stages of these waves (see Appendix A, Figures A.1 and A.2).
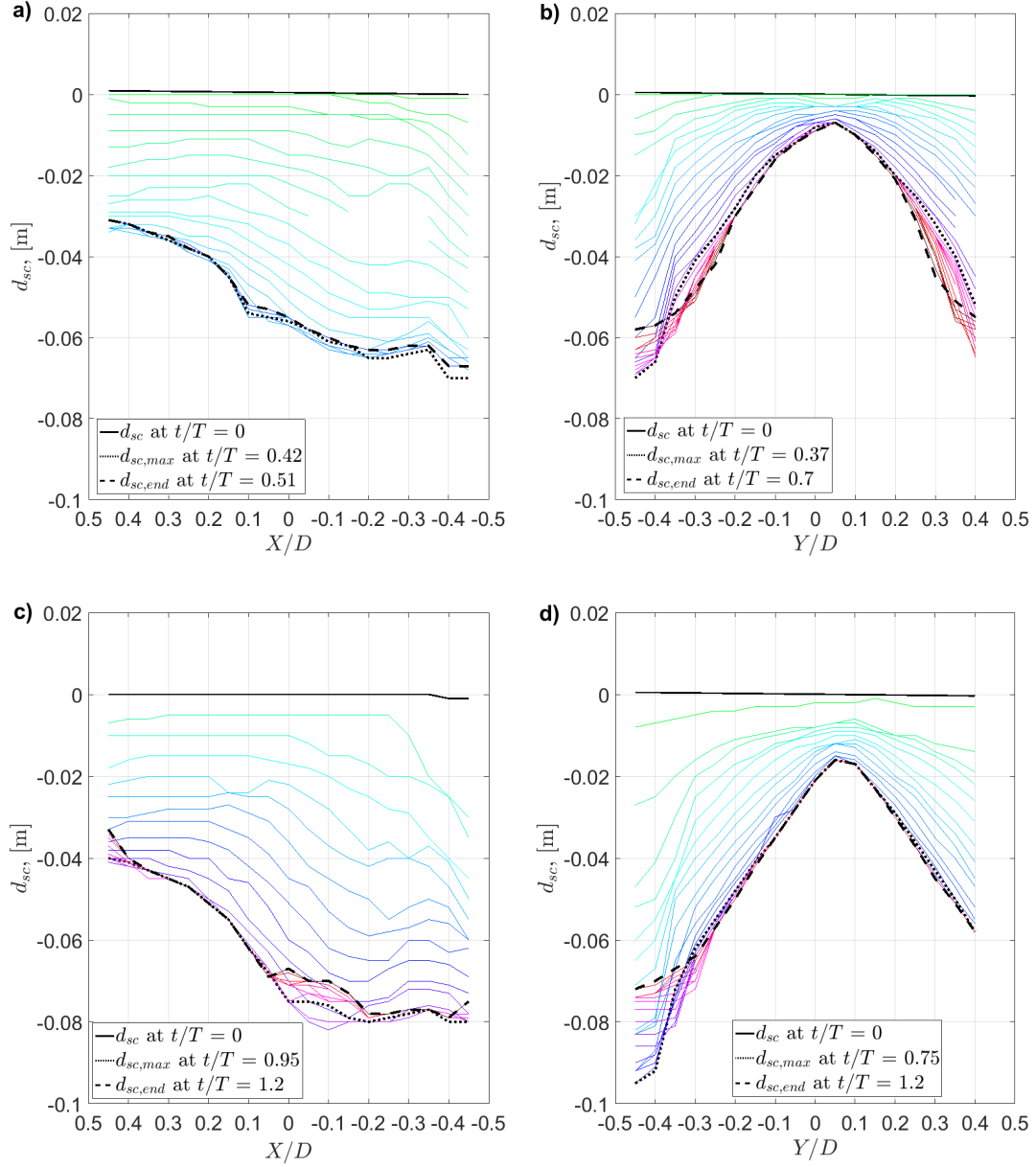
Figure 11: a-d. The development of scour at the side (Figure 11a, c), and front faces (Figure 11b, d) of the structure during the TL49a (top row) and CL25a (bottom row) waves. Bed level readings are taken every 1 s ($t/T = 0.023$) and 0.5 s ($t/T = 0.02$) for the TL49 and CL25 waves respectively. The time at which $d_{sc,max}$ and $d_{sc,end}$ are achieved is highlighted.

25

442   Further discussion on the role of the horseshoe vortex can be made by comparing the
443   observed process of scour with published literature. Tonkin et al. (2003) cases I and II for un-
444   submerged and partially submerged cylinders in sand, respectively, show the horseshoe vortex
445   to be a significant scouring phenomena in the early stages of solitary wave inundation. Its
446   formation is from the downward flow momentum caused by the plunging breaker just before
447   the cylinder. Lavictoire (2014) also observe the horseshoe vortex to be present during bore
448   impacts with the structure. In the current tests, the CL25 waves have already broken, and
449   impact the structure led by a small broken front. The TL49 and CL147 waves do not break,
450   and do not exhibit a discernible broken wave front upon impact. It seems, therefore, that in
451   the current tests the horseshoe vortex is less important in the scour process, particularly for
452   the CL147 waves.

453   *3.3. Time Development and Equilibrium*

454   The recorded time development of scour is now discussed. For all waves live-bed con-
455   ditions prevail with $\theta > \theta_{cr}$. While velocity data is not available throughout the entire
456   inundation process, video and visual observations during the tests reveal that rippling of
457   the bed starts immediately after inundation begins for all waves. Despite the prevalence of
458   live-bed conditions, it does not appear that equilibrium is achieved in any test, due to the
459   triangular scour hole shape.

460   Figure 12a-b shows $d_{sc,max}$ versus $d_{sc,end}$ at the side face and front face for all tests
461   and structures, respectively. In all waves and locations $d_{sc,max} > d_{sc,end}$, in agreement with
462   observations from Nakamura et al. (2008). The raw values are given in Table 2 along with
463   the percentage differences between $d_{sc,max}$ and $d_{sc,end}$ for all waves.

464   The CL147 waves produce the greatest scour. For this wave $KC = 281$, indicating that
465   despite the flow velocity being lower than that of the CL25 waves ($\bar{U} = 0.382$ and 0.666
466   m/s respectively) and comparable to that of TL49 waves (where $\bar{U}$ ranges between 0.324 -
467   0.334 m/s, Table 1), the inundation time (i.e., T) is much longer than both. This means
468   that the scouring flow field has a longer period of time to entrain sediment from the bed and
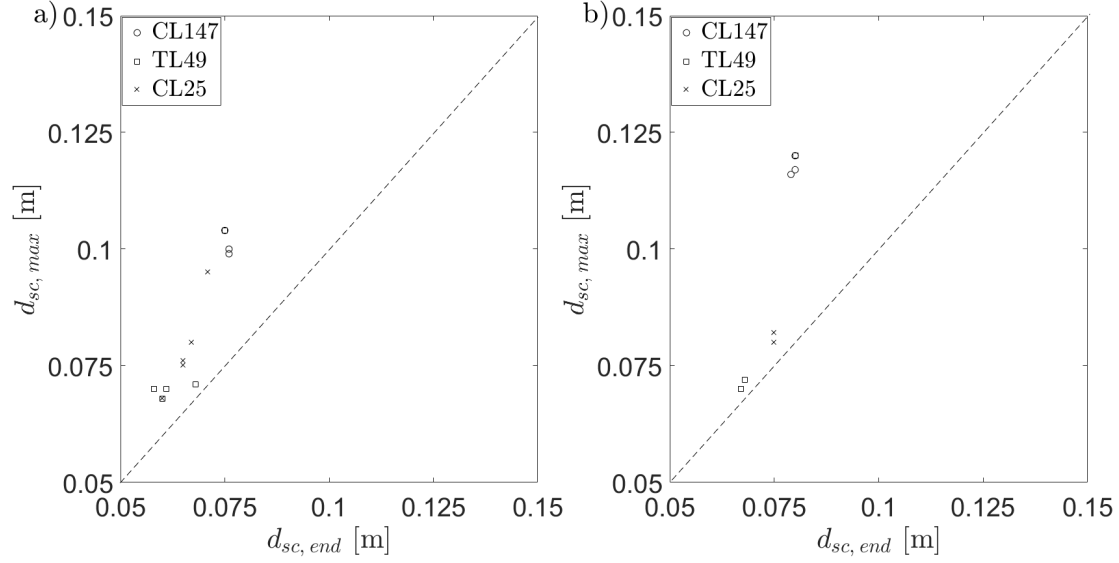469   transport downstream.

26

Figure 12: a-b. $d_{sc,max}$ versus $d_{sc,end}$ at the corner positions of a), the front face ($Y/D = -0.45, X/D = -0.5$) and b), side face ($Y/D = -0.5, X/D = -0.45$) of the structures for all tests.

470   Figure 13 shows the normalised scour depth d_{sc}/D as a function of t/T for CL147a,
471 TL49a and CL25a. These are typical of the repeated runs for each wave period. For CL147a
472 $d_{sc}/D(t)$ along the centreline position follows an exponential scour development curve similar
473 to that observed in unidirectional scour (e.g., Melville and Coleman 2000). The rate at the
474 front corner location on the side face (X/D = -0.45, Y/D = -0.5, where $d_{sc,max}$ is recorded),
475 however, exhibit non-linearity in the scour process. This is manifest as a less smooth curve in
476 comparison to centreline. The non-linearity is significant at this position due to the presence
477 of the lateral base-vortex. Here, the scour rate decreases until the maximum scour depth
478 $d_{sc,max}/D$ occurs at $t/T \approx 0.57$, after which slumping occurs. (Note, this value of t/T is not
479 equal to that on Figure 9, which only includes measurements at intervals of $t/T = 0.04$).
480 The centreline curve indicates the fastest rate of scour occurs at $t/T \approx 0.5$, coinciding with
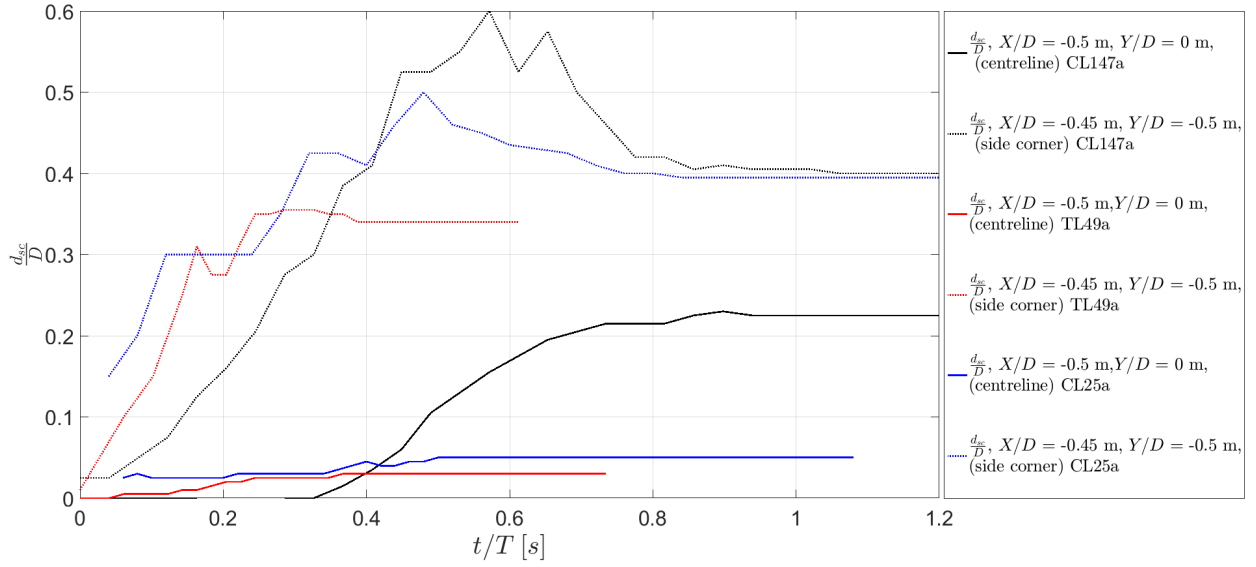481 h_{max}.

27

Figure 13: Centreline and side face corner scour time development curves for the CL147a, TL49a and CL25a wave runs at Structure 1.

For the TL49a wave run, the scour development is relatively more irregular that for the CL147a at all positions. This is likely a due to the shorter and more turbulent nature of the inundation. The majority of the scouring occurs in the 1st third of the inundation. $d_{sc,max}/D$ occurs earlier in the inundation time in comparison to the CL147a wave above, at $\approx t/T = 0.33$, after which a small amount of slumping occurs again. Scour at the centreline is minimal, reaching a maximum of $0.03D$ and no slumping is observed. $d_{sc}/D(t)$ for the CL25a wave reaches a maximum at $\approx t/T = 0.48$ and slumping occurs immediately after. As with all other waves, the corner scour is much greater than the centreline. No slumping occurs at the centreline and $d_{sc,max}/D$ is limited to $0.05D$.

It is uncertain whether equilibrium can be attained during single tsunami wave inundation. Progress to equilibrium will primarily be driven by the tsunami duration to time scale of scour ratio, which for a single tsunami inundation will likely be low. The equilibrium depth for a given onshore structure may, therefore, only be achieved after several inundation and return flows such as during a tsunami wave train event. Larsen et al. (2018) observed equilibrium in their offshore tsunami cases was achieved only after approximately 50 waves, suggesting that it may take numerous waves to achieve equilibrium onshore as well. Knowledge of the inundation and return flow durations can be used to estimate whether equilibrium will be achieved in a given tsunami event. In such cases where a small number of tsunami

28

waves inundate onshore in one tsunami event, scour may be better characterised by the spatial and temporal location of $d_{sc,max}$, the change in d_{sc} around the structure (which may influence the structure dynamic response to hydrostatic and hydrodynamic loading) and $d_{sc,end}$.

3.4. Comparison of Results with Prediction Equations

Recorded $d_{sc,max}$ for each test and structure is here compared to well-known empirical equilibrium scour depth (d_{sce}) predictor equations. The comparison is made with the caveat that such equations are developed for either waves, or currents only, and for the case of offshore / fully wetted scenarios.

For waves, currents and combined wave and currents, d_{sce} is equivalent to $d_{sc,end}$ which is defined when, for example, the depth of scour increases by less than 5% in 24 hours (Melville 1997). d_{sce} is generally equal or similar to $d_{sc,max}$. However, $d_{sc,max}$ in live-bed conditions, tidal flows and waves is not necessarily equal to d_{sce}. In such scenarios the periodic passing of ripples through the scour hole and/or changes in flow direction may cause $d_{sc,max}$ to vary by a small amount around the mean value given by d_{sce}. For the purposes of the comparison below, $d_{sc,max}$ is assumed to equal d_{sce}.

The Colorado State University equation (CSU, Equation 9) as cited in the HEC-18 Evaluating scour at bridges (Richardson and Davis, 2001) commissioned by the US Federal Highway Administration is widely used to calculate the equivalent $d_{sc,max}$ for cylindrical structures in a unidirectional steady current scenario.

$$\frac{d_{sc,max}}{D} = 2K_1K_2K_3K_4 \left(\frac{h}{D}\right)^{0.35} F_r^{0.43} \tag{9}$$

where K_1 = correction factor for pier shape (1.1 for square nosed), K_2 = correction factor for angle of attack of flow (1 for 0°), K_3 = correction factor for bed condition (1.1 for small dunes / plane bed), K_4 = correction factor for bed armouring (1 for narrow graded sand). Correction factor values are determined from Tables 6.1-6.3 in Richardson and Davis (2001). For the present tests, the flow parameters are derived at X/D = -5.5.

For $d_{sc,max}$ in waves, the influence of KC number is illustrated in Figure 11 of Sumer et al. (1992) which shows d_{sc}/D as a function of KC. Sumer et al. (1992) show that for KC approximately $> 10^2$, d_{sc}/D approaches an asymptote of 1.3, as given by Equation 10.

$$\frac{d_{sc,max}}{D} = 1.3(1 - exp(-0.03(KC - 6))), \quad \text{for} \quad KC > 6 \tag{10}$$

29

530   Sumer et al. (1993) conducted experiments to investigate the effect of cross-section on
531 scour as a function of KC. They determined the empirical expression show in Equation 11
532 for $d_{sc,max}/D$ for a square structure oriented 90° to the incident wave in live-bed conditions.
533 Such a scenario is the most relevant to the current tests.

$$534 \qquad \frac{d_{sc,max}}{D} = 2(1 - exp(-0.015(KC - 11))), \quad \text{for} \quad KC > 11 \qquad (11)$$

535   The (ASCE, 2016) Tsunami Loads and Effects design codes present a simple empirical
536 prediction model for onshore tsunami induced scour. This is based on post tsunami field
537 surveys of scour holes around structures (see Tonkin et al. 2013). An envelope of scour depth
538 is provided based on the inundation height h. This is $d_{sc,max} = 1.2h$ for $h < 3.05$ m and
539 $d_{sc,max} = 3.66$ m for $h > 3.05$ m. The (ASCE, 2016) predictions are included in Table 2. As
540 h in all waves in the model is > 3.05 m at 1:50 scale, the predicted scour depth is therefore
541 3.66 m which at 1:50 scale is 0.0732 m.

542   Figure 14 shows $\frac{d_{sc,max}}{D}$ recorded at the side face of the structures as a function of a),
543 T and b), KC. The predicted $\frac{d_{sc,max}}{D}$ from Equations 9, 10, 11 and ASCE (2016) are also
544 plotted. The raw values including $d_{sc,max}$ and $d_{sc,end}$ are given in Table 2 and KC numbers
545 in Table 1. Focussing on the side face which gives the larger scour depths as opposed to
546 the front face, the value of $d_{sc,max}$ for the CL147 waves is less than half that predicted
547 from Equations 9 and 10 (respectively 0.258 m and 0.26 m, Figures 14a and b). $d_{sc,max}$
548 is over three times less than that predicted by Equation 11 (0.39 m, Figure 14b). Over-
549 predictions are present for the TL49 and CL25 waves also. For the TL49 waves, the ASCE
550 (2016) performs well (Figure 14a). For the CL25 and CL147 waves, the ASCE (2016) under
551 predicts $d_{sc,end}$, but only by a relatively small amount (Table 2). However, a critical finding
552 of these experiments is that $d_{sc,max}$ is in some cases up to a third greater than $d_{sc,end}$. Thus
553 the use of the ASCE (2016) prediction, which is based on post-tsunami scour observations
554 of $d_{sc,end}$ may lead to undesirable underestimations of $d_{sc,max}$, which may occur earlier in the
555 inundation. The ASCE (2016) prediction does not account for variables that are known to
556 influence scour, such as flow velocity, KC number, and structure diameter. Based on the
557 current limited data, it is difficult to conclude over which ranges of these parameters, use of
558 the ASCE (2016) will lead to an under-prediction of scour.

Table 2: All $d_{sc,max}$ and $d_{sc,end}$ values for each wave and structure. Additionally the percentage difference between the two is given, along with the predicted $d_{sc,max}$ using Equations 9, 10, 11 and ASCE (2016).

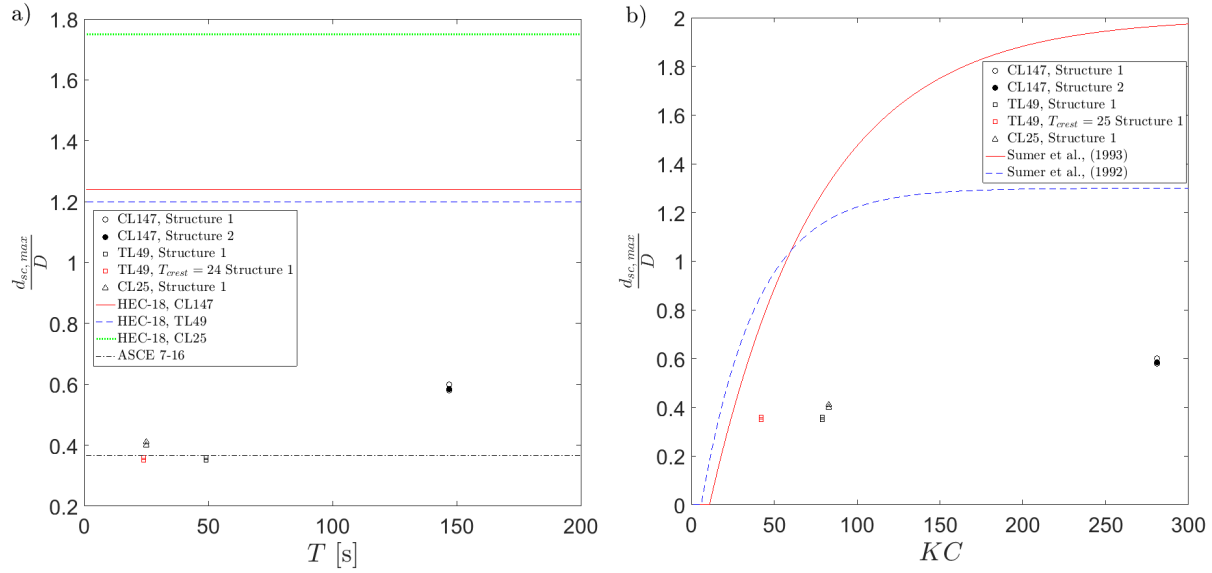| Wave Run	Struc-ture	Front face $Y/D = -0.45$ $d_{sc,max}$ [m]	$d_{sc,end}$ [m]	% reduction from $d_{sc,max}$	Side face $X/D = -0.45$ $d_{sc,max}$ [m]	$d_{sc,end}$ [m]	% reduction from $d_{sc,max}$	HEC-18 Equation 9 [m]	Sumer et al. (1992) Equation 10 [m]	Sumer et al. (1993) Equation 11 [m]	ASCE predic-tion [m]
CL147a	1	-	-	-	0.12	0.08	33	0.25	0.26	0.39	
CL147a	2	0.1	0.076	24	0.117	0.08	32	0.25	0.26	0.39	
CL147b	1	0.099	0.076	23	0.116	0.079	32	0.25	0.26	0.39	
CL147c	1	0.104	0.075	28	0.12	0.08	33	0.25	0.26	0.39	
TL49a	1	0.07	0.058	17	0.07	0.067	4	0.24	0.23	0.26	0.0732
TL49a	2	0.071	0.068	6	-	-	6	0.24	0.23	0.26	
TL49b	1	0.07	0.061	13	0.072	0.068	-	0.24	0.23	0.26	
TL49b	2	0.068	0.06	12	-	-	9	0.24	0.23	0.26	
CL25a	1	0.08	0.067	16	0.082	0.075	-	0.35	0.23	0.26	
CL25a	2	0.075	0.065	13	-	-	6	0.35	0.23	0.26	
CL25b	1	0.095	0.071	25	0.08	0.075	-	0.35	0.23	0.26	
CL25b	2	0.076	0.065	14	-	-		0.35	0.23	0.26	

Figure 14: a), $d_{sc,max}/D$ as a function of T at the side faces of the structures for all waves and, b), $d_{sc,max}/D$ plotted as a function of KC at the side faces of the structures respectively. The appropriate predictor equations are also shown. T_{crest} is the period of the crest of the TL49 waves and is discussed in Section 3.5.

The TL49 and CL25 waves produce similar $d_{sc,max}$ and have similar KC numbers (of 79 - 83, Figure 14, also Tables 1 and 2). CL147 has a larger KC (281) and $d_{sc,max}$ than both. The results are in line with the expected influence of KC, however, the values are significantly lower than those expected from Equation 10 and 11. This certainly suggests that equilibrium scour depth is not achieved, and it may also be stipulated that the KC number may not be the only appropriate variable for tsunami inundation. Wind wave scour is strongly related to KC as it describes the orbital motion of the fluid which alternates the flow direction during each period, and therefore, the temporal duration and strength of the main scouring phenomena during each period. The orbital motion of the wave is less apparent in tsunami inundation, however. While the inundation is driven by the incoming wave, it is hypothesised that the wave energy is significantly dissipated through bed friction and the overland return flow (though not modelled in these tests) is likely more similar to open channel surface flow governed by gravity.

3.5. Comparison of Results with Published Experimental Data

By comparing the experimental data with appropriate published data, the influence of inundation height and duration on the scour depth can be investigated. The experimental

data of Nakamura et al. (2008), Lavictoire (2014) and Shafiei et al. (2015) are the most comparable studies to the current experiments. Nakamura et al. (2008) conducted tests of 'long waves' and solitary waves. These over-topped a sea wall to scour at an onshore square structure, and as such are the most similar to the current tests. The maximum period tested was 14 s. Lavictoire (2014) studied the inundation of bores with a circular structure in sand and gravel beds. Shafiei et al. (2015) observed bore inundation and scour around square, diamond and circular structures in sand beds, focussing on the effect of foundation depth of the structure.

Figure 15 shows $d_{sc,end}/D$ as a function of h/D where h represents the over-topping height for the case of Nakamura et al. (2008), the bore depth for Lavictoire (2014) and Shafiei et al. (2015), and inundation depth in the current tests. These are equivalent measurements that describe the water depth at the structure in all four set-ups. The current tests include $d_{sc,end}/D$ recorded from the side corners of Structure 1 and the front face corner of Structure 2 (where the side view is unavailable). The CL25 waves which are the shortest period tested, plot just above the edge of the Nakamura et al. (2008) 'long wave' data, indicating a greater scour depth for the increase in period. The longer period TL49 and CL147 data also show greater $d_{sc,max}/D$ for lower inundation heights than the Nakamura et al. (2008) 'long wave' data which suggests that scour is sensitive to the duration of inundation. In the current tests $\theta > \theta_{cr}$; the longer these live-bed conditions prevail, the faster the instantaneous rate of scour, and larger the overall volume of sediment transport will be.

The CL147 and the TL49 waves plot closer to those of the Lavictoire (2014) and Shafiei et al. (2015) bores over sand and gravel beds of similar h/D. There are differences to be noted between the three investigations, however, which fundamentally look at two different types of inundation on different shape structures (circular for Lavictoire 2014). The primary difference is in the wave type; the current tests being unbroken cyclic inundation from a long wave, as opposed to turbulent bore front inundation followed by a gradual reduction in inundation height and velocity for Lavictoire (2014) and Shafiei et al. (2015). The velocities of the bores are significantly higher than the inundation velocities in the current tests. The overall length of inundation is comparable to the current tests, but the duration of the bore fronts themselves is short, and comparable to the Nakamura et al. (2008) 'long waves' (where maximum $T = 14$ s). The similarity in $d_{sc,max}/D$ as a function of h/D between the current data, Lavictoire (2014) and Shafiei et al. (2015), all three of which have significantly greater inundation time of the Nakamura et al. (2008) 'long wave' study, further suggests the length

33

of the inundation has bearing on the amount of scour.

It is also apparent from the data that the inundation time has more influence than the inundation height. The effective inundation period of the TL49 waves, (i.e., the period of the crest $T_{crest} \approx 25$ s) is the same as the CL25. However, h in TL49 is approximately half the value, and yet $d_{sc,end}/D$ is only slightly lower. This is also despite $\bar{U}$ being double for the CL25 waves. Further, $d_{sc,end}/D$ for the TL49 waves is significantly greater than the equivalent the Nakamura et al. (2008) 'long wave' crest-led data at equivalent h/D. Nakamura et al. (2008) also concluded that inundation duration had a greater influence than inundation height by comparing their solitary wave data to their 'long wave' data, the latter showing greater $d_{sc,end}/D$. The long inundation time of the CL147 waves enables the scouring flow field to become more fully established and suspend and transport more sediment from the structures locality than the shorter waves.
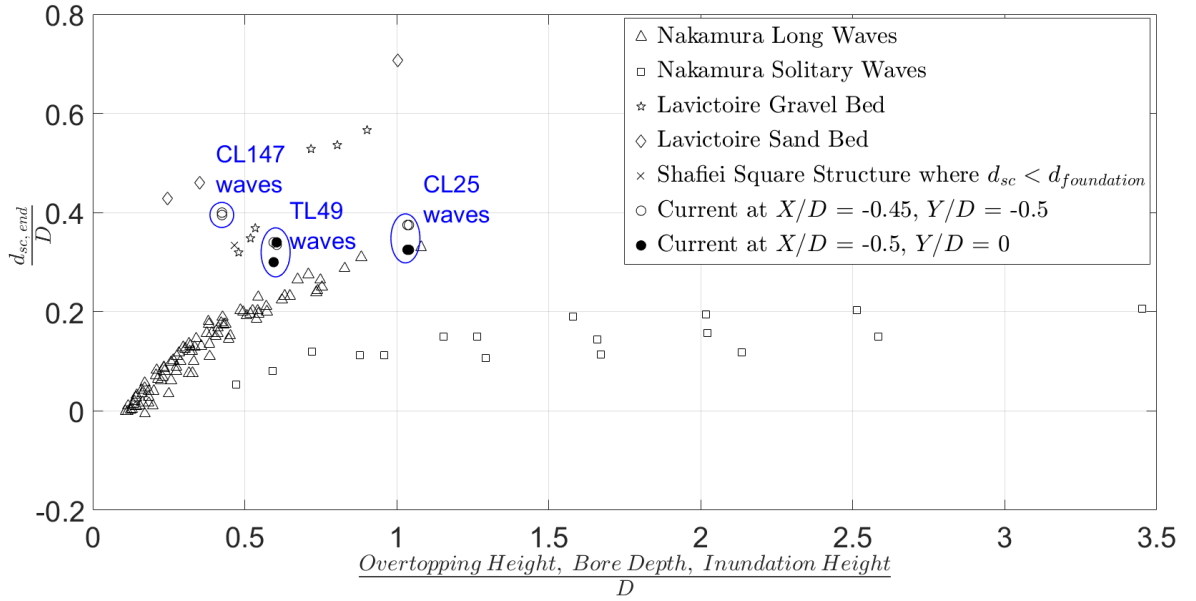

Figure 15: $d_{sc,end}/D$ as a function of equivalent h/D for the current data and selected published experiments (see legend). The data from Shafiei et al. (2015) includes only that which is comparable to the current study. This is where the depth of the foundation $d_{foundation} > d_{sc,max}$ in that study.

4. Conclusions

The scour development and depth due to the inundation of tsunami length long waves at an onshore square structure is investigated. Three waves periods are tested; crest-led 147

34

s and 25 s, and a trough-led 49 s wave. These waves propagate over a 1:20 slope before impinging on a flat sediment pit in which a square structure is placed.

The results indicate that the rate of onshore scour development varies with time due to the changes in flow velocity and depth. Larger scour depths were observed to be more dependent upon inundation time than velocity. Maximum scour depths occur at approximately $\frac{2}{3}T$, with the exception of the CL25. Slumping is observed towards the end of inundation, in some cases reducing the final scour depth by $\frac{1}{3}$ of its maximum. Therefore, scour depths inferred from post tsunami field surveys may underestimate the maximum scour depth.

Scour depths at the leading corner of the structure are up to 33% greater than at the centreline, indicating that equilibrium is not achieved during a single tsunami wave inundation. Additionally, the data is compared against empirical predictions which tend to over-predict the scour, further suggesting equilibrium is not achieved. While tsunami may involve subsequent inundations and return flows, the usefulness of the theoretical equilibrium scour depth as a measure of tsunami scour is as yet uncertain. More important variables are likely to be the spatial and temporal location of $d_{sc,max}$, the differential of d_{sc} around the structure (which may dynamically affect its response to loading) and $d_{sc,end}$.

To expand the data presented which is limited to three wave periods, it is compared with suitable published data. This enables the investigation of the effect of h, KC and inundation duration on the scour. It is shown that the inundation duration appears to most influence the scour depth. The influence of h is less apparent, while KC influence is not necessarily the same as observed for wind wave and current scour. This is stipulated to be due to transition of tsunami from wave-like to current-like flows during inundation.

Design guidelines for tsunami scour at onshore structures need to account for the transient nature of $d_{sc,max}$ over the full period of inundation in order to accurately identify the greatest scour depth a structure may experience during inundation, which must influence the forces felt by the structure and its overall stability. This will include quantification of the spatial and temporal location of $d_{sc,max}$ and the instantaneous variation of d_{sc} around the structure. Additional investigations should look to refine this, investigating further the influence of h, KC and duration to give a more robust empirical prediction method for tsunami scour. Additionally, the return flow should be investigated. If the mechanism is similar to tidal scour (e.g., McGovern et al. 2014) but on a shorter time-scale then the return flow is likely to cause scour on the opposite side of the structure. McGovern et al. (2014) observed infilling on the shoreward side initially, before an increasing scour depth at all sides. For solitary

wave inundation of a circular cylinder, Tonkin et al. (2003) showed the most significant scour occurred due to a large vertical gradient in pore water pressure at the rear of the cylinder during the return flow. This, along with the influence of variations in sediment and structure, should be investigated.

5. Acknowledgements

ASCE (2016). *ASCE/SEI 7-16 Chapter 6: Tsunami Loads and Effects.*

Bricker, J. D., Francis, M., and Nakayama, A. (2012). Scour depths near coastal structures due to the 2011 Tohoku tsunami. *Journal of Hydraulic Research*, 50(6):637–641.

Brown, J. (2013). *Waves, Tides and Shallow Water Processes.* Elsevier.

Chen, B. and Li, S. (2018). Experimental study of local scour around a vertical cylinder uner wave-only and combined wave-current conditions in a large-scale flume. *Journal of Hydraulic Engineering*, 144(9).

Chock, G., Robertson, S. E., Kriebel, D., Francis, M., and Nistor, I. (2013). *Tohoku, Japan, Earthquake and Tsunami of 2011.* ASCE.

EEFIT (2004). The Indian Ocean tsunami of 26 December 2004 mission findings in Sri Lanka and Thailand. Technical report, Institution of Structural Engineers.

EEFIT (2011). The mw 9.0 Tohoku Earthquake and Tsunami of 11th March 2011. Technical report, Institution of Structural Engineers.

Ettema, R. (1980). *Scour at Bridge Piers.* PhD thesis, University of Auckland.

684 Foster, A. S. J., Rossetto, T., and Allsop, W. (2017). An experimentally validated approach
685   for evaluating tsunami inundation forces on rectangular buildings. *Coastal Engineering*,
686   128:44–57.

687 Fritz, H. M., Borrero, J., Synolakis, C. E., and Yoo, J. (2006). 2004 Indian Ocean tsuanmi
688   flow velocity measurements from survivor videos. *Geophysical Research Letters*, 33.

689 Fuhrman, D. R., Schløer, S., and Sterner, J. (2013). Rans-based simulation of turbulent
690   wave boundary layer and sheet-flow sediment transport processes. *Coastal Engineering*,
691   73:151–166.

692 Hjorth, P. (1975). Studies on the nature of local scour. Technical Report 46, University of
693   Lund, Sweden.

694 Jayaratne, M. P. R., Premaratne, B., Adewale, A., Mikami, T., Matsuba, S., Shibayama,
695   T., Esteban, M., and Nistor, I. (2016). Failure mechanisms and local scour at coastal
696   structures induced by tsunami. *Coastal Engineering Journal*, 58(4).

697 Kajitani, Y., Chang, S. E., and Tatano, H. (2013). Economic impacts of the 2011 Tohoku-Oki
698   Earthquake and Tsunami. *Earthquake Spectra*, 29(S1):S457–S478.

699 Kawai, H., Satoh, M., Kawaguchi, K., and Seki, K. (2013). Characteristics of the 2011
700   Tohoku tsunami waveform acquired around Japan by nowphas equipment. *Coastal Engi-*
701   *neering Journal*, 55(3).

702 Larsen, B. E., Arboll, L. K., Kristoffersen, S. F., Carstensen, S., and Fuhrman, D. R. (2018).
703   Experimental study of tsunami-induced scour around a monopile foundation. *Coastal*
704   *Engineering*, 129:36–49.

705 Larsen, B. E., Fuhrman, D. R., Baykal, C., and Sumer, B. M. (2017). Tsunami-induced
706   scour around monopile foundations. *Coastal Engineering*, 129:36–49.

707 Lavictoire, A. (2014). Bore-induced local scour around a circular structure. Master's thesis,
708   Department of Civil Engineering, University of Ottawa.

709 Madsen, P., Fuhrman, D., and Schäffer, H. (2008). On the solitary wave paradigm for
710   tsunamis. *Journal of Geophysical Research*, 113(C12012).

McGovern, D. J., Ilic, S., Folkard, A. M., McLelland, S. J., and Murphy, B. J. (2014). Time development of scour around a cylinder in simulated tidal currents. *Journal of Hydraulic Engineering*, 140(6).

McGovern, D. J., Robinson, T., Chandler, I. D., Allsop, W., and Rossetto, T. (2018). Pneumatic long-wave generation of tsunami-length waveforms and their runup. *Coastal Engineering*, 138:80–97.

Mehrzad, S., Nistor, I., and Rennie, C. D. (2016). Experimental modeling of supercritical flows-induced erosion around structures. In *Proceedings of the 6th International Conference on the Application of Physical Modelling in Coastal and Port Engineering and Science (Coastlab16)*.

Melville, B. W. (1997). Pier and abutment scour integrated approach. *Journal of Hydraulic Engieering*, 123(2).

Melville, B. W. and Coleman, S. E. (2000). *Bridge Scour*. Water Resources Publications, CO.

Mori, N. and Takahashi, T. (2012). The 2011 Tohoku Earthquake and Tsunami joint survey group. Nationwide post event survey and analysis of the 2011 Tohoku Earthquake and Tsunami. *Coastal Engineering Journal*, 54:1–27.

Nakamura, T., Kuramitsu, Y., and Mizutani, N. (2008). Tsunami scour around a square structure. *Coastal Engineering Journal*, 50(2):209–246.

Pan, C. and Huang, W. (2012). Numerical modeling of tsuanmi wave run-up and effects on sediment scour around a cylindrical pier. *Journal of Engineering Mechanics*, 138(10):1224–1235.

Rabinovich, A. B. and Thomson, R. E. (2007). The 26 december 2004 Sumatra tsunami: analysis of tide gauge data from the world ocean part 1. Indian Ocean and South Africa. *Pure and Applied Geophysics*, (164):261–308.

Richardson, E. V. and Davis, S. R. (2001). Evaluating scour at bridges. Hydraulic Engineering Circular no. 18. Technical report, Federal Highway Administration, Washington, DC.

Rossetto, T., Allsop, W., Charvet, I., and Robinson, D. (2011). Physical modelling of tsunami using a new pneumatic wave generator. *Journal of Coastal Engineering*, 58:517–527.

Saha, A. K. (2013). Unsteady flow past a finite square cylinder mounted on a wall at low reynolds number. *Computers and Fluids*, 88:599–615.

Shafiei, S., Melville, B. W., Shamseldin, A. Y., Watts, M. J. H., and Hoffman, T. G. (2015). Experimental investigation of tsunami bore induced scour around structures. In *Australian Coasts and Ports Conference*.

Sheppard, D. M., Melville, B., and Demir, H. (2014). Evaluation of existing equations for loal scour at bridge piers. *Journal of Hydraulic Engineering*, 140(1):14–23.

Soulsby, R. L. and Whitehouse, R. J. S. (1997). Threshold of sediment motion in coastal environments. In *Pacific Coasts and Ports '97: Proceedings of the 13th Australasian Coastal and Ocean Engineering Conference and the 6th Australasian Port and Harbour Conference*, volume 1.

Sumer, B. M., Christiansen, N., and Fredsøe, J. (1993). Influence of cross section on wave scour around piles. *Journal of Waterway, Port, Coastal and Ocean Engineering*, 119(5):477–495.

Sumer, B. M., Fredsoe, J., and Christiansen, N. (1992). Scour around vertical pile in waves. *Journal of Waterway, Port, Coastal, and Ocean Engineering*, 118(1):15–31.

Sumer, B. M., Fredsoe, J., and Christiansen, N. (2001a). Scour around a pile in combined waves and current. *Journal of Hydraulic Engineering*, 127(5).

Sumer, B. M., Whitehouse, R. J., and Torum, A. (2001b). Scour around coastal structures: a summary of recent research. *Coastal Engineering*, 44(2):153–190.

Tadepalli, S. and Synolakis, C. (1994). The runup of N-waves. *Proceedings of the Royal Society*, A 445:99–112.

Telford, J., Cosgrave, J., and Houghton, R. (2006). Synthesis report: Joint evaluation of the international response to the Indian Ocean tsunami. Technical report, Tsunami Evaluation Coaliton (TEC).

Tonkin, S., Yeh, H., Kato, F., and Sato, S. (2003). Tsunami scour around a cylinder. *Journal of Fluid Mechanics*, 496:165–192.

Tonkin, S. P., Francis, M., and Bricker, J. D. (2013). Limits on coastal scour depths due to tsunami. In Davis, C., Du, X., Miyajima, M., and Yan, L., editors, *International Efforts in Lifeline Earthquake Engineering*, volume TCLEE 38.

Whitehouse, R. J. S. (1998). *Scour at Marine Structures*. Thomas Telford.

Williams, I. A. and Fuhrman, D. R. (2016). Numerical simulation of tsunami-scale wave boundary layers. *Coastal Engineering*, 110:17–31.

Wilson, R., Davenport, C., and Jaffe, B. (2012). Sediment scour and deposition within harbors in california (USA), caused by the March 11, 2011 Tohoku-Oki tsunami. *Sedimentary Geology*, 282:228–240.

Yeh, H., Franci, M., Peterson, C., Katada, T., Latha, G., Chadha, R. K., Singh, J. P., and Raghuraman, G. (2007). Effects of the 2004 Great Sumatra Tsunami: Southeast Indian Coast. *Journal of Waterway, Port, Coastal and Ocean Engineering*, 133(6):382–400.

Yoshii, T., Tanaka, S., and Matsuyama, M. (2017). Tsunami deposits in a super-large wave flume. *Marine Geology*, 391:98–107.

Yoshii, T., Tanaka, S., and Matsuyama, M. (2018). Tsunami inundation, sediment transport, and deposition process of tsunami deposits on coastal lowland inferred from the tsunami sand transport laboratory experiment (TSTLE). *Marine Geology*, 400:107–118.

Appendix A.

Figures A.1 and A.2 show the front face of Structure 2 during test CL25b and TL49b respectively. Note the significantly more turbulent and suspended sediment opposed to the CL147 waves given in Figure 8.
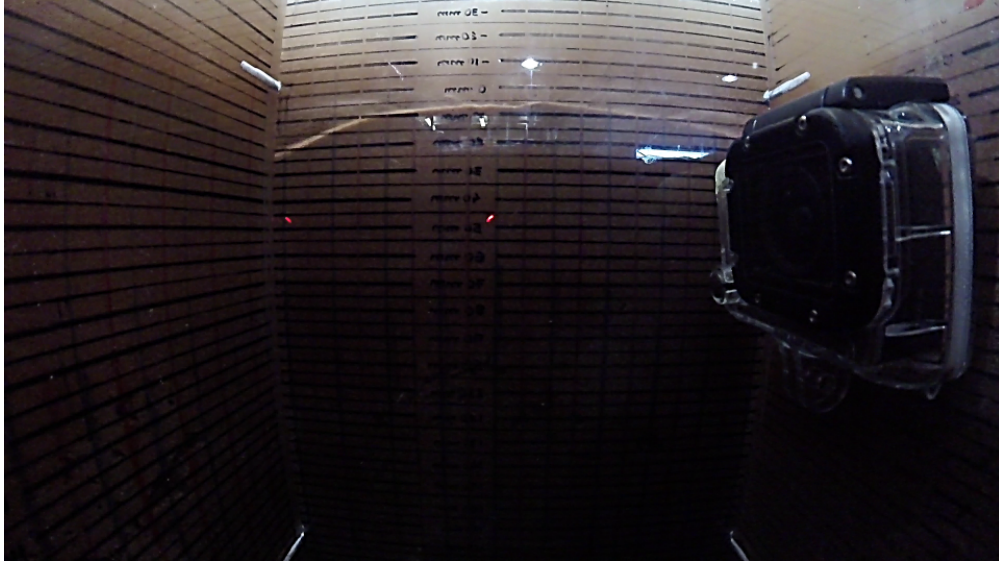
Figure A.1: Image still from the front facing GoPro during the early stages of the CL25b inundation on Structure 2 showing a significant amount of suspended sediment.
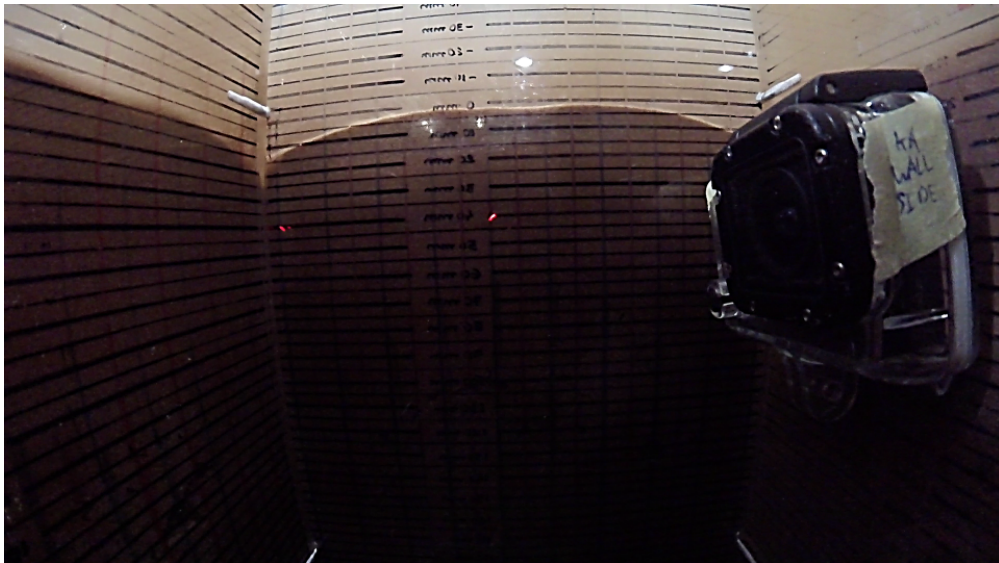

Figure A.2: Image still from the front facing GoPro during the early stages of the TL49b inundation on Structure 2 showing a significant amount of suspended sediment.